

Continuum approximation of dyking with a theory for poro-viscoelastic–viscoplastic deformation

Yuan Li¹,^{*} Adina E. Pusok,¹ Timothy Davis,¹ Dave A. May² and Richard F. Katz¹

¹*Department of Earth Sciences, University of Oxford, Oxford, OX1 3AN, UK. E-mail: yuan.li@earth.ox.ac.uk,*

²*Institute of Geophysics and Planetary Physics, Scripps Institution of Oceanography, University of California San Diego, La Jolla, CA 92093, USA*

Accepted 2023 April 17. Received 2023 April 17; in original form 2022 December 5

SUMMARY

To reach Earth's surface, magma must ascend from the hot, ductile asthenosphere through cold and brittle rock in the lithosphere. It does so via fluid-filled fractures called dykes. While the continuum mechanics of ductile asthenosphere is well established, there has been little theoretical work on the cold and brittle regime where dyking and faulting occurs. Geodynamic models use plasticity to model fault-like behaviour; plasticity also shows promise for modelling dykes. Here we build on an existing model to develop a poro-viscoelastic–viscoplastic theory for two-phase flow across the lithosphere. Our theory addresses the deficiencies of previous work by incorporating (i) a hyperbolic yield surface, (ii) a plastic potential with control of dilatancy and (iii) a viscous regularization of plastic failure. We use analytical and numerical solutions to investigate the behaviour of this theory. Through idealized models and a comparison to linear elastic fracture mechanics, we demonstrate that this behaviour includes a continuum representation of dyking. Finally, we consider a model scenario reminiscent of continental rifting and demonstrate the consequences of dyke injection into the cold, upper lithosphere: a sharp reduction in the force required to rift.

Key words: Fracture and flow; Plasticity, diffusion, and creep; Numerical modelling; Continental tectonics: extensional; Mechanics, theory, and modelling; Physics of magma and magma bodies.

1 INTRODUCTION

Terrestrial volcanoes are fed by magma produced in and extracted from the hot, ductile, asthenosphere. To arrive at shallow depths, this magma ascends through the lithosphere, which ranges from ductile at its base to elastic–brittle near its cold, upper surface. The observed character of lavas, of solidified magmatic intrusions and of volcanic regions more broadly are typically explained in terms of the structure of magma storage and transport pathways through the lithosphere (Cashman *et al.* 2017; Magee *et al.* 2018; Edmonds *et al.* 2019). Furthermore, magma–lithosphere interaction along these pathways profoundly influences the mechanical properties of the lithosphere, especially at divergent tectonic boundaries (Kendall *et al.* 2005; Wright *et al.* 2012). The effect of magma within the lithosphere is believed to be a leading-order control on mechanics of plate tectonics (Buck 2006; Bialas *et al.* 2010).

To understand and describe the nature of lithospheric melt transport requires a conceptual framework that links disparate observations, including lava chemistry, topography, gravity, seismic structure and kinematics of plate boundaries. The framework must comprise mechanics, heat transport and petrology and must be valid across a range of homologous temperatures from nearly zero to unity. It must accommodate the mechanics of solids, liquids

and their interactions, from viscous compaction in the hot mantle (McKenzie 1984) to fluid-driven brittle fractures in the cold crust (Rivalta *et al.* 2015). Crucially, the conceptual framework should elucidate the transition between these hot and cold mechanical regimes (Katz *et al.* 2022)—a ductile–brittle transition that must exist within the lithosphere. This latter requirement is a major challenge for two key reasons: first, that mechanical properties of the solid are sensitive to temperature, leading to behaviour that varies sharply with time scale of stress changes and position in the thermal structure and, secondly, that this thermal structure is itself modified by magma transport and phase change within it.

Quantitative theoretical models are useful for establishing and exploring this conceptual framework, and for making testable predictions. The purpose of this work is to develop a mathematical theory for the mechanics of magma transport across the lithosphere. Building on the work of Keller *et al.* (2013), we aim to create a tractable mathematical framework that captures the ductile, elastic and brittle deformation of the lithosphere and their coupled behaviour associated with liquid magma. Crucially, our framework should capture dyking, a key brittle process for magma transport in the lithosphere, and its interaction with faulting (and ductile shear zones) as well as ductile compaction and porous flow of melt.

Dykes, like faults, are thin. When viewed in relation to the scale of elastic or ductile deformation, they are effectively 2-D discontinuities embedded in a 3-D solid continuum. They form and evolve at timescales that are much shorter than timescales of thermal diffusion or viscous adjustment of the solid (Lister 1994; Rubin 1998). Hence their mechanics have typically been investigated under conditions of fixed forcing (e.g. static far-field stresses, Dahm 2000; Muller *et al.* 2001). Indeed, these separations of scale make it difficult to consistently couple dykes within models of continuum, tectonic-scale deformations. However, it is clear from the observations that such coupling is crucial for the natural evolution of tectonic boundaries (Buck 2006; Bialas *et al.* 2010).

1.1 Incorporating discontinuous deformation in continuum models

To approximate this coupling and investigate its consequences, two approaches can be considered. The first is to model dykes as discrete features that overlay a continuum model. In this case, dykes appear either when certain conditions are met (e.g. Buck 2004, 2006) or at a location chosen on an empirical basis (e.g. Liu & Buck 2018). The discrete dykes are coupled by exchange of mass, momentum and/or energy with the continuum (though this ‘exchange’ is sometimes implemented as a one-way coupling). An advantage of this approach is that it can respect the scale separation: dykes can appear or evolve at time- and length-scales that are far below that of the spatio-temporal grid used to discretize the continuum problem. A disadvantage is that consistent, two-way coupling between the continuum and discrete features (i.e. dykes) is difficult or impossible. The assumptions needed to make the coupling tractable limit the space of possible model outcomes.

The second approach is to capture dykes at the level of partial differential equations, in a manner similar to previous work that simulates faults in geodynamic models (e.g. Naliboff *et al.* 2017, 2020). Such single-phase, viscous, incompressible geodynamic models approximate faults by enrichment of the constitutive law. In particular, previous workers have represented brittle failure and frictional sliding in terms of plasticity, whereby the strength of the continuum drops sharply when/where a critical stress (the yield stress) is reached (Fullsack 1995; Moresi & Solomatov 1998; Tackley 2000). The advantage of this approach is that the continuum faults are fully and consistently coupled in the framework of the conservation statements. A disadvantage is the potential ill-posedness of the problem, which may occur when pressure-dependent flow laws are used (Lanzendörfer 2011). Ill-posedness is associated with a loss of ellipticity (Renardy 1986; Lanzendörfer 2011) and results in mesh-dependent solutions and a lack of convergence of the non-linear solver algorithm (due to solution non-uniqueness, Spiegelman *et al.* 2016). The underlying reason is the absence of spatial and temporal scales of yielding in a plasticity model without an appropriate regularization (Borst & Duretz 2020).

In single-phase, viscoplastic models, Duretz *et al.* (2019) showed that a plastic regularization can resolve this issue. The regularization smears the zones of plastic failure in space and time such that they are resolved by a numerical solution [i.e. their behaviour is independent of grid refinement (Miehe *et al.* 2010; Duretz *et al.* 2019)]. While this has the benefit of stabilizing simulations, it inevitably represents a discontinuity in displacements as a continuous zone of plastic yielding. Nonetheless, it appears to be a valuable tool, enabling the use of continuum plasticity to approximate brittle failure and frictional sliding.

1.2 Overview of our strategy

Here we take the continuum-based approach and, guided by the pioneering work of Rozhko *et al.* (2007) and Keller *et al.* (2013), we extend it for modelling dykes within the lithosphere. In particular, we propose a rheological model combining viscosity, elasticity and plasticity into a two-phase flow context. This model addresses key shortcomings of Keller *et al.* (2013) (a critical review of that paper is provided in Section 2.1). Our theory then has three key distinctions from Keller *et al.* (2013): we propose (i) a plastic yield function and (ii) a plastic potential function that prevent non-physical predictions under tensile plastic failure at vanishing shear stress. Also, (iii), we introduce a regularization to ensure that plastic yielding can be resolved after discretization.

Regarding differences (i) and (ii), we adopt a plastic-yield surface that is a smooth conjunction of Griffith and Drucker–Prager criteria, originally proposed by Carol *et al.* (1997). Its hyperbolic form is asymptotic to the Drucker–Prager model, as we show in the next section. This form is compatible with an associative plastic potential, but we propose a more flexible form with a tunable dilatancy parameter. This form can recover the associative plastic potential in one limit and, in the other limit, it enforces zero dilatancy for an incompressible, single-phase flow.

Regarding difference (iii), we adopt the regularization proposed by Duretz *et al.* (2019) and elaborated by Duretz *et al.* (2021), replacing the simple plastic element in a Maxwell-composite constitutive law with a Kelvin viscoplastic element. The resulting viscoelastic–viscoplastic composite is shown in Fig. 1(a). At plastic failure, the Kelvin dashpot provides a rate-dependent resistance that distributes shear stress (and plastic failure) over a finite-width zone. The width of this zone is controlled by the viscosity η^K of the Kelvin dashpot (Duretz *et al.* 2021). Our results support the effectiveness of this approach but elsewhere that effectiveness has been debated, at least for the case where inertia is not negligible (Stathas & Stefanou 2022). Other works use a micropolar Cosserat formulation (e.g. Rudge 2021) that introduces an inherent length scale and regularizes the localization of deformation (Iordache & Willam 1998). However, this comes at the expense of adding a biharmonic (fourth-order) term to the force-balance equation.

We incorporate our rheological formulation into a two-phase-flow theory and show that it exhibits plastic behaviour that is representative of faulting and dyking. We emphasize the plastic representation of dyking and demonstrate its quantitative correspondence with linear elastic fracture mechanics. Finally, we consider a model scenario reminiscent of continental rifting and demonstrate the mechanical consequences of dyke injection into the cold, upper lithosphere: a sharp reduction in the force required to rift.

The paper is organized as follows. In Section 2, we describe a poro-viscoelastic–viscoplastic (poro-VEVP) composite constitutive law for a two-phase continuum. After a review of Keller *et al.* (2013) in Section 2.1, we present basic theory for the constitutive law in Section 2.2. The extensions of Keller’s work are highlighted in Sections 2.3–2.4. Section 2.5 completes the rheological model by including the relations between material properties and porosity. To understand the evolution of stresses in a poro-VEVP material, Section 2.6 presents an analysis of the system of ordinary differential equations representing local stress evolution for given strain rates. In Section 3, we present the system of conservation equations and, in Section 3.1, their discretization. In Section 3.2, we present numerical solutions in idealized configurations, and compare results with predictions of linear elastic fracture mechanics. In Section 3.3, we present solutions in a configuration inspired by continental rifting.

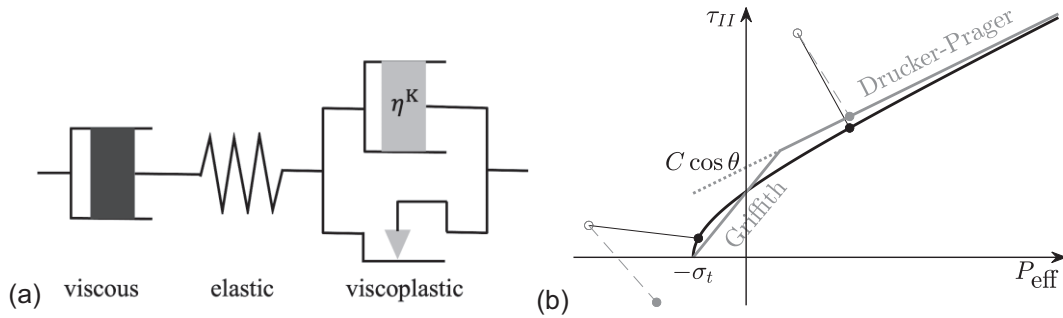


Figure 1. Overview of the rheological model. (a) Schematic diagram of the viscoelastic-viscoplastic (VEVP) rheological model. The Kelvin viscous dashpot is labelled η^K . (b) Yield surfaces in the space of effective pressure and the second invariant of the shear stress. The grey lines show the piece-wise linear Griffith-Drucker-Prager (GDP) yield surface from Keller *et al.* (2013); the black curve is the proposed hyperbolic yield surface. The hyperbolic curve is asymptotic to the Drucker-Prager yield surface at large stresses. The dotted line extends Drucker-Prager to a y-intercept at $C \cos \theta$, where C is the cohesion and θ is the friction angle. Two states of stress (open circles) are predicted by assuming a viscoelastic rheological model. These are then corrected onto each of the two yield surfaces (filled circles) assuming associative plasticity. For the case with lower predicted τ_{II} , the plastic correction to the GDP yield envelope produces a non-physical, negative value of τ_{II} .

We then conclude the paper with a discussion of our method and results (Section 4) and a condensed summary (Section 5).

2 RHEOLOGICAL MODEL OF PORO-VISCOELASTIC-VISCOPLASTIC ROCK

The general mathematical context of mass and momentum conservation for partially molten rocks was established by McKenzie (1984) and others [a comprehensive introduction with references is available in Katz (2022)]. However, that work focuses on the partially molten asthenosphere, which responds to stress only by viscous creep. While this may be an adequate description of the asthenosphere on long timescales, it is not general enough to model the lithosphere, where homologous temperatures range to near zero and brittle-elastic responses to stress are evident. Keller *et al.* (2013) addresses this deficiency by proposing a poro-viscoelastic-plastic formulation of the isotropic and deviatoric parts of the constitutive law.

2.1 A review of Keller *et al.* (2013)

Motivated by the same questions of lithospheric melt transport considered here, Keller *et al.* (2013) presents the first theory for two-phase flow with a rheological model of the solid that combines viscosity, elasticity and plasticity. In their theory, when the stress is below the yield stress of the plastic element, the constitutive law is viscoelastic and the total strain rate is the sum of the viscous and elastic rates. The elastic part is evaluated in terms of the Jaumann derivative to capture stress evolution objectively, independent of reference frame. It is then written in a semi-discretized form to enable the derivation of an effective viscosity that represents the full rheological model.

The limit of pure viscoelastic deformation is the plastic-yield stress. Keller *et al.* (2013) parametrizes the plastic-yield stress as a function of the effective pressure. In their eq. (37), Keller *et al.* (2013) combines Drucker-Prager and Griffith criteria in a piece-wise linear yield surface, reproduced with a grey solid line in Fig. 1(b). A prescribed tensile strength of the solid phase sets a minimum effective solid pressure; at effective pressures less than this negative value, plastic failure can occur in the absence of shear

stress. These negative effective pressures can be achieved by liquid overpressure. At effective solid pressures above this minimum, plastic yielding can be attained with sufficient shear stress.

If stress reaches the plastic-yield threshold, then the effective viscosity is reduced accordingly to keep the stress on the yield surface. However, Keller *et al.* (2013) does not specify a plastic potential, which leaves ambiguity in how the plastic flow is calculated.

This formulation enables Keller *et al.* (2013) to obtain numerical solutions in which poro-viscoelastic deformation co-exists with continuum approximations of dykes, sills and faults—all interacting consistently within the conservation-law framework. Their ground-breaking, proof-of-concept results demonstrated the potential to model melt transport across the lithosphere. However, deficiencies in certain details of the theoretical formulation require ‘hacks’ in the numerical implementation to stabilize solutions. Two of these deficiencies are salient here. First, the lack of plastic regularization leads to mesh dependence (Duretz *et al.* 2019) and non-uniqueness of the solution, resulting in poor (or non-)convergence of the non-linear solver (Spiegelman *et al.* 2016). Secondly, the form of the plastic-yield function and the absence of a plastic potential can lead to non-physical stresses during tensile failure. This situation is illustrated in Fig. 1(b) and detailed in Appendix A, where liquid overpressure with vanishing shear stress drives the system to yield, and then the plastic potential drives the second invariant of the shear stress to become negative. This results in a spurious, negative effective viscosity.

In the following subsections, we propose our remedies for these deficiencies: a Kelvin viscoplastic regularization for the rheological model, a hyperbolic yield surface for the plastic model and an explicitly defined plastic potential function.

2.2 Strain rate decomposition

To set the scene, we briefly review the key physics relevant to establish the rheological models for a solid-liquid aggregate. Closure of the conservation equations requires a relationship between the effective stresses (deviatoric and isotropic) of the aggregate and the velocity field of the solid phase; both stress types require their own constitutive laws. Formally, we seek the relations for $(1 - \phi)\boldsymbol{\tau}$ and $(1 - \phi)\Delta P$ in terms of the solid strain rate tensor. Here, we have introduced the following notation: $\boldsymbol{\tau}$ is the deviatoric stress tensor of the solid; ΔP is the pressure difference between the solid and

liquid phase; ϕ is the local volume fraction of the melt (i.e. porosity). The factor of $(1 - \phi)$ arises from the fact that in an arbitrary cut through the two-phase medium with a contiguous solid matrix, the solid phase supports the full effective stress but covers a portion of the area assumed to be equal to its volume fraction.

Similar to Keller *et al.* (2013), we assume a Maxwell rheological model that combines viscous, elastic and (visco)plastic strain rates, as shown in Fig. 1(a) (for the moment, we set aside our use of a Kelvin viscoplastic element). With this configuration, each of the three rheological units is subject to the same stress, but each accommodates a different strain rate. The strain rate of each rheological element contributes to the total strain rate $\dot{\mathbf{E}}$. To formally define the constitutive behaviour for the shear (deviatoric) and volumetric (isotropic) stresses, we adopt the decomposition

$$\dot{\mathbf{E}} = \dot{\mathbf{e}} + \frac{1}{3}\dot{C}\mathbf{I}, \quad (1)$$

where $\dot{\mathbf{e}}$ and \dot{C} are the deviatoric and isotropic strain rates given by

$$\dot{\mathbf{e}} = \dot{\mathbf{E}} - \frac{1}{3}\text{Tr}(\dot{\mathbf{E}})\mathbf{I}, \quad \dot{C} = \text{Tr}(\dot{\mathbf{E}}), \quad (2)$$

where $\text{Tr}(\cdot)$ denotes the trace operator. Using these terms, the strain rate decomposition is given by

$$\dot{\mathbf{e}}^v + \dot{\mathbf{e}}^e + \dot{\mathbf{e}}^{vp} = \dot{\mathbf{e}}, \quad (3)$$

$$\dot{C}^v + \dot{C}^e + \dot{C}^{vp} = \dot{C}, \quad (4)$$

where the superscripts v , e , vp denote the viscous, elastic and (visco)plastic strain rates. \dot{C} is often referred to as the compaction rate (although compaction is $\dot{C} < 0$ so \dot{C} should more properly be called the decompression rate).

For the viscous element, the deviatoric and isotropic strain rates take the following constitutive relations,

$$\dot{\mathbf{e}}^v = \frac{(1 - \phi)\dot{\boldsymbol{\tau}}}{2\eta_\phi}, \quad \dot{C}^v = -\frac{(1 - \phi)\Delta P}{\zeta_\phi}, \quad (5)$$

where η_ϕ and ζ_ϕ are the shear and compaction viscosity, respectively. For the elastic element, the corresponding constitutive relations are

$$\dot{\mathbf{e}}^e = \frac{(1 - \phi)\dot{\boldsymbol{\tau}}}{2G_\phi}, \quad \dot{C}^e = -\frac{(1 - \phi)\Delta \dot{P}}{Z_\phi}, \quad (6)$$

where G_ϕ , Z_ϕ are the shear and drained bulk modulus, respectively, and $\dot{\boldsymbol{\tau}}$, $\Delta \dot{P}$ denote the time rate of change of the deviatoric stress and the interphase pressure difference respectively. The subscript ϕ indicates a dependence on porosity; these are made explicit in Section 2.5.

For the (visco)plastic element, we incorporate a plastic theory that is capable of addressing both shear and tensile failure (e.g. Murrell & Digby 1970a, b). Both modes of failure are expressed in terms of the shear stress and the plastic-effective pressure of the solid phase. The plastic-effective pressure is the same as the solid pressure when there is no liquid (Murrell & Digby 1970a); otherwise it is the pressure difference between solid and liquid (Murrell & Digby 1970b). Either scenario is possible in a partially molten rock. In order to consistently capture both scenarios, we define the plastic-effective pressure of the solid phase, P_{eff} , as

$$P_{\text{eff}} = \Delta P + (1 - \alpha_p)P^l, \quad \text{where } \alpha_p = \exp(-\phi_p/\phi), \quad (7)$$

where P^l is the liquid pressure and ϕ_p is a porosity threshold across which α_p smoothly transitions from 1 to 0. This causes P_{eff} to change from being equal to the interphase pressure difference ($P_{\text{eff}} = \Delta P = P^s - P^l$) to being equal to the solid pressure ($P_{\text{eff}} = \Delta P + P^l = P^s$). A justification of eq. (7) is presented in Appendix B. Where ϕ

= 0 there is no liquid present but we nonetheless set $P^l = P^s$ for mathematical consistency.

The stress state within a material that undergoes plastic deformation is described by a yield function \mathcal{F} . During yielding, $\mathcal{F} = 0$; otherwise its value must be negative. A stress state for which $\mathcal{F} < 0$ implies that the material is not subject to plastic failure and therefore $\dot{\mathbf{e}}^{vp} = 0$.

When plastic flow occurs, a plastic potential function uniquely determines the direction of (visco)plastic flow. Given a plastic potential Q ,

$$\dot{\mathbf{e}}^{vp} = \dot{\lambda} \frac{\partial Q}{\partial \boldsymbol{\tau}}, \quad \dot{C}^{vp} = -\dot{\lambda} \frac{\partial Q}{\partial P_{\text{eff}}}, \quad (8)$$

where $\dot{\lambda}$ is the plastic multiplier, representing the magnitude of the plastic strain rate. Our formulation for the yield function \mathcal{F} and the potential function Q are presented in Sections 2.3 and 2.4.

2.3 Plastic regularization and the yield function

To address the issues of mesh-dependence and loss of ellipticity associated with plastic failure, we follow Duretz *et al.* (2019) and introduce a plastic regularization. This takes the form of a viscous element in a Kelvin composite with the plastic element, as shown in Fig. 1(a). Elements of a Kelvin body share a common deformation rate, but contribute additive stresses. Combining the Kelvin viscoplastic element with viscous and elastic elements in a Maxwell series in the context of two-phase flow, the rheological model becomes a poro-VEVP law. Duretz *et al.* (2019, 2020), Borst & Duretz (2020) and Duretz *et al.* (2021) have shown that this VEVF formulation provides mesh-independent plastic shear failure in a single-phase, (in)compressible Stokes model. We extend the application of this rheological model to our two-phase model. Furthermore, we use it to capture not only shear failure but also tensile failure.

The essence of the poro-VEVP model is to consider this Kelvin viscoplastic composite as one unit that possesses a rate-dependent yield function \mathcal{F} , defined as

$$\mathcal{F}(\dot{\lambda}, P_{\text{eff}}, \tau_{II}) = F(P_{\text{eff}}, \tau_{II}) - \eta^K \dot{\lambda} \leq 0, \quad (9)$$

where η^K is the viscosity of the dashpot in the Kelvin body, F denotes a rate-independent yield function of the plastic element and $\tau_{II} = \sqrt{\boldsymbol{\tau} : \boldsymbol{\tau}/2}$ is the second invariant of the shear stress tensor of the solid phase. The rate-dependent yield function \mathcal{F} inherits the yield criterion from F . However, unlike standard plasticity theory, F can be greater than zero. Indeed it is this overstress that balances the resistance of the viscous element in the Kelvin body and ensures that $\mathcal{F} \leq 0$. When $\mathcal{F} < 0$ there is no plastic deformation; then, $\dot{\lambda} = 0$ and only the viscous and elastic elements in the Maxwell composite contribute to the strain rates. Otherwise, when $\mathcal{F} = 0$ plastic flow occurs and $\dot{\lambda} > 0$.

The formulation (9) stems from the Perzyna model for Kelvin viscoplasticity (Perzyna 1966) and is further developed as a consistency model in Wang *et al.* (1997) and Heeres *et al.* (2002).

To capture both shear and tensile failure within the same framework, we propose a rate-independent plastic yield function that has the form of a hyperbola,

$$F(P_{\text{eff}}, \tau_{II}) = \sqrt{\tau_{II}^2 + (C \cos \theta - \sigma_t \sin \theta)^2} - (C \cos \theta + P_{\text{eff}} \sin \theta), \quad (10)$$

where C is the cohesion, σ_t is the tensile strength and θ is the angle of internal friction (black solid line in Fig. 1b). We treat these

parameters as constants here, but their values can be allowed to vary with the accumulated plastic strain to implement a model of strain softening/hardening (as in Section 3.3). A similar form was proposed by Carol *et al.* (1997) for a discrete crack analysis in an elastoplastic material; it was extended by Lorefine *et al.* (2008) as a rate-dependent form for Kelvin viscoplasticity.

A hyperbolic yield function has several key benefits. First, when the associative plastic law applies, $Q = F$, it resolves the issue existing in the piece-wise Drucker–Prager–Griffith yield function (i.e., that non-physical stresses can result from tensile failure, as discussed in Section 2.1 and explained in Appendix A). This improvement makes the whole plastic theory mathematically consistent. Secondly, a smooth yield surface avoids the computational complexity associated with the discontinuity of slope where the two linear parts of the yield surface intersect (Simo *et al.* 1988). Thirdly, it promotes convergence of the numerical scheme, especially when using a Newton-type non-linear solver that favours smooth variation of variables.

Fig. 1(b) illustrates the yield surface of eq. (10). At the limit of zero shear stress, eq. (10) becomes

$$F = -(P_{\text{eff}} + \sigma_t) \sin \theta \quad \text{for } \tau_{II} = 0, \quad (11)$$

which is the classical Griffith criterion. For a sufficiently large shear stress, eq. (10) becomes

$$F \sim \tau_{II} - (C \cos \theta + P_{\text{eff}} \sin \theta) \quad \text{for } \tau_{II} \gg C \cos \theta - \sigma_t \sin \theta, \quad (12)$$

which is the Drucker–Prager plastic envelope.

For convenience, we introduce the notation τ_y to represent the shear-stress threshold for yield. Independent of the Kelvin viscous element, plastic yielding takes place when $\tau_{II} = \tau_y$. When the Kelvin viscosity is present, τ_{II} can increase beyond this threshold; otherwise it is limited to τ_y . For the hyperbolic function (10), the yield criterion is

$$\tau_y = [(C \cos \theta + P_{\text{eff}} \sin \theta)^2 - (C \cos \theta - \sigma_t \sin \theta)^2]^{1/2}. \quad (13)$$

2.4 Plastic potential function

Following the suggestion in Carol *et al.* (1997), we choose the potential function,

$$Q(P_{\text{eff}}, \tau_{II}) = \sqrt{\tau_{II}^2 + (C \cos \theta - \sigma_t \sin \theta)^2} - (C \cos \theta + c_{dl} P_{\text{eff}} \sin \theta), \quad (14)$$

which includes a dilatancy coefficient $c_{dl} \in [0, 1]$. In the case of $c_{dl} = 0$, no dilatancy occurs. This is useful for describing an incompressible, single-phase material. At the other end-member $c_{dl} = 1$, we recover the associative plastic law that $\partial Q / \partial P_{\text{eff}} = \partial F / \partial P_{\text{eff}}$. Our use of the word dilatancy follows the definition in Carol *et al.* (1997): the decompaction of the solid phase associated with any plastic failure (Carol *et al.* 1997, refers to decompaction as crack opening). We also follow Carol *et al.* (1997) for the choice of the values of c_{dl} that include the two limiting values and the transition between them: the associative plastic law at $c_{dl} = 1$ and zero dilatancy at $c_{dl} = 0$.

In this work we define c_{dl} via the following porosity dependent relationship

$$c_{dl} = \exp(-\phi_c / \phi), \quad (15)$$

which provides a smooth transition between $c_{dl} = 0$ and 1 in terms of ϕ . The threshold for the transition ϕ_c is a model parameter.

We acknowledge the non-linear form of the plastic-yield and plastic-potential functions proposed by Yarushina *et al.* (2020).

Their approach leads to a topologically different yield curve than ours. In particular, whereas our curve has $\tau_{II} = 0$ at only one value of $P_{\text{eff}} < 0$, theirs has two distinct values of P_{eff} where $\tau_{II} = 0$; one of these has $P_{\text{eff}} < 0$ and the other has $P_{\text{eff}} > 0$. This form, while empirically relevant under some circumstances (e.g. Bedford *et al.* 2019), has not been used for geodynamic models. Instead, these typically posit a form similar or identical to the Drucker–Prager plastic envelope at sufficiently large P_{eff} .

The analysis in Appendix A shows that this plastic model with a hyperbolic yield surface resolves the issue of non-physical stress during tensile failure that was associated with the piece-wise linear yield surface.

2.5 Porosity dependence of material properties

The shear and volumetric viscosity assume the following forms:

$$\eta_\phi = \eta_0 \exp(-\beta\phi), \quad \zeta_\phi = \eta_0 \phi^{-1}, \quad (16)$$

where η_0 is the reference shear viscosity. Here the reference viscosity η_0 refers to the shear viscosity associated with the purely viscous (creep) flow law and thus may be a function of temperature, strain rate and pressure. Mei *et al.* (2002) shows empirically that $26 \leq \beta \leq 31$. In this paper, we choose $\beta = 27$. The maximum value of ζ_ϕ is limited according to $\zeta_\phi \leq 10^3 \eta_0$ to ensure ζ_ϕ remains bounded when $\phi \rightarrow 0$. A minimum value of η_ϕ is imposed as $\eta_\phi \geq 10^{-3} \eta_0$ to preserve the solver convergence as $\phi \rightarrow 1$.

The shear and bulk moduli are given by

$$G_\phi = G_0(1 - \phi), \quad Z_\phi = Z_0(1 - \phi)\phi^{-1/2}, \quad (17)$$

where G_0 is a reference value when $\phi = 0$; Z_0 is a chosen prefactor. The factor $(1 - \phi)$ in both G_ϕ , Z_ϕ ensures that the elastic stress response to the strain rate of the solid phase decreases to zero when the porosity increases to one. The value of Z_ϕ is restricted to be less than a chosen dimensional value $Z_\phi \leq Z_{\text{max}}$ in order to bound Z_ϕ when $\phi \rightarrow 0$.

2.6 Point-wise stress evolution under constant strain rates

Here we analyse the evolution of stresses of the solid phase at a material point (e.g. a single point in physical space) where the poro-VEVP rheological model applies. We then perform a controlled numerical experiment in which we impose the strain rates $\dot{\mathbf{E}}$ and hold them constant. Similarly we also assume ϕ is a constant. In this context, the stresses vary due to the viscous relaxation of the elastic energy and the constraints of the plastic model. We aim to focus attention on the distinct behaviour of the Kelvin viscoplastic body and hence to analyse the simplest instance of the rheological formulation.

To proceed, the constitutive laws (eqs 5 and 6) together with the plastic model (eq. 8) are substituted into eqs (3) and (4). Assuming a constant strain rate and porosity and aligning the coordinate system so that only $\dot{\epsilon}_{xy}$ is non-zero, we obtain two ordinary differential equations (ODEs) for $\tau_{II}(t)$ and $\Delta P(t)$,

$$\dot{\tau}_{II} + \frac{G_\phi}{\eta_\phi} \tau_{II} + \frac{2G_\phi \dot{\lambda}}{(1 - \phi)} \frac{\partial Q}{\partial \tau_{II}} = \frac{2G_\phi}{(1 - \phi)} \dot{\epsilon}_{II}, \quad (18)$$

$$\Delta \dot{P} + \frac{Z_\phi}{\zeta_\phi} \Delta P + \frac{Z_\phi \dot{\lambda}}{(1 - \phi)} \frac{\partial Q}{\partial P_{\text{eff}}} = \frac{-Z_\phi}{(1 - \phi)} \mathcal{C}. \quad (19)$$

Substituting the plastic potential (eq. 14) into these ODEs and combining the yield condition (eq. 9) with the hyperbolic yield function (eq. 10), we seek solutions for $\tau_{II}(t)$ and $\Delta P(t)$ for the chosen values

of $\dot{\epsilon}_{II}$ and \mathcal{C} . In the simplest cases, analytical solutions exist; these are useful to understand the qualitative behaviour of the rheological model.

We start by investigating two cases: a pure-shear flow without dilatancy and a pure-compaction flow. For the pure-shear case we impose a constant, non-zero $\dot{\epsilon}_{II}$ and take $\mathcal{C} = 0$ along with $\phi = c_{dl} = 0$. With these choices $\Delta P = 0$ and the evolution of τ_{II} is governed solely by eq. (18). For the pure-compaction case we impose a constant, non-zero \mathcal{C} and take $\dot{\epsilon}_{II} = 0$, $\phi \neq 0$. Accordingly $\tau_{II} = 0$ and the evolution of ΔP is then governed solely by eq. (19). These two cases are solved numerically and compared with the analytical results presented below. The dimensional parameter values used for this section are listed in Table 1. $\dot{\epsilon}_{II}$ is the same for all cases in this section.

Fig. 2(a) shows the evolution of τ_{II} for a pure-shear flow at three different values of η^K . Before yielding, all three of these results match with the analytical solution for a viscoelastic flow,

$$\tau^{ve} = \tau_0 [1 - \exp(-t/t_{Mw})], \quad (20)$$

where $\tau_0 = 2\eta_\phi \dot{\epsilon}_{II} / (1 - \phi)$ is the long-term viscous stress (in the absence of plastic failure) and $t_{Mw} = \eta_\phi / G_\phi$ is the Maxwell time for shear deformation.

The yielding threshold is attained at $\tau_{II} = \tau_y$, independent of the value of the Kelvin viscosity η^K (τ_y is defined in eq. 13). Fig. 2(a) shows that the stress after yielding depends on η^K . When $\eta^K = 0$ (black dots), the stress remains exactly equal to the yield stress. This is the case of a viscoelastic–plastic rheological model. For $\eta^K > 0$, the shear stress τ_{II} increases beyond τ_y toward an asymptotic value that is determined by the value of η^K . This long-term stress is written implicitly in eq. (C3).

The timescale for approaching asymptotic stress after plastic yielding is associated with a VEPV Maxwell time. This is the timescale for the relaxation of elastic stress by the combined deformation of the intrinsic and Kelvin viscous elements. It cannot be obtained analytically for a hyperbolic yield surface. However, for large τ_{II} , the hyperbolic yield surface is asymptotic to the Drucker–Prager criterion, as in eq. (12). Using this linear approximation, the VEPV Maxwell time is given as

$$\tilde{t}_{Mw} = \left[\frac{G_\phi}{\eta_\phi} + \frac{2G_\phi}{\eta^K(1-\phi)} \right]^{-1} = \frac{t_{Mw}}{1 + 2\eta_\phi / [\eta^K(1-\phi)]}, \quad (21)$$

as shown in Appendix C. In Fig. 2(a), the short vertical lines indicate a time after yielding $t - t_{yield} = 4\tilde{t}_{Mw}$, when the stress is <1 per cent lower than the asymptotic value. The gradual increase in stress after yielding is the consequence of an internal timescale for plastic failure, quantified by \tilde{t}_{Mw} , which arises from the Kelvin-viscoplastic rheological element.

Fig. 2(b) shows a similar pattern for the evolution of ΔP in a pure-compaction flow with an imposed, constant value of \mathcal{C} and $\dot{\epsilon}_{II} = 0$. Note that for simplicity in this section we assume constant porosity, even under compaction flow. Before yielding, the curves for the compaction stress ΔP match the viscoelastic analytical solution,

$$\Delta P^{ve} = -\Delta P_0 [1 - \exp(-t/t_{Mw}^C)], \quad (22)$$

where $\Delta P_0 = \zeta_\phi \mathcal{C} / (1 - \phi)$ is the magnitude of the long-term viscous stress (in the absence of yielding) and $t_{Mw}^C = \zeta_\phi / Z_\phi$ is the Maxwell time for viscoelastic compaction. Here, we have taken the porosity to be large enough that $\alpha_p = 1$ in eq. (7). Thus, $P_{eff} = \Delta P$ and the yield threshold is $\Delta P = -\sigma_t$.

In this case, analytical solutions for VEPV compaction are plotted in Fig. 2(b) and given by eq. (C9) in Appendix C. Also in this appendix, the VEPV Maxwell time for compaction after yielding is

determined exactly as

$$\tilde{t}_{Mw}^C = \left[\frac{Z_\phi}{\zeta_\phi} + \frac{Z_\phi \sin^2 \theta}{\eta^K(1-\phi)} \right]^{-1} = \frac{t_{Mw}^C}{1 + \zeta_\phi \sin^2 \theta / [\eta^K(1-\phi)]}. \quad (23)$$

This is the timescale after yielding for the compaction stress to evolve to its asymptotic value. The short vertical lines in Fig. 2(b) indicate $t - t_{yield} = 4\tilde{t}_{Mw}^C$.

From panels (a) and (b) of Fig. 2 it is evident that when $\eta^K > 0$, the asymptotic maximum stress is greater than the yield threshold. We refer to this difference as the excess stress [note that it is different from the commonly used term ‘overstress’, which is $\eta^K \dot{\lambda}$ (Wang *et al.* 1997; Heeres *et al.* 2002; Duretz *et al.* 2019)]. Panel (c) plots the excess stress as a function of η^K , showing that the excess stress increases approximately linearly with the Kelvin viscosity for both pure shear and compaction flow. Solutions are obtained analytically as eqs (C3) and (C4) (for pure-shear flow, the analytical solution is implicit). For comparison, an explicit analytical result is also obtained in the Drucker–Prager limit.

Fig. 2(d) plots the solutions to eqs (18) and (19) in the P_{eff} – τ_{II} plane for three different forcing cases: shear without compaction (red), compaction without shear (blue) and mixed-mode (green). Stress evolves in the direction of the arrow. For each forcing case, three rheological scenarios are considered. The first, shown by a thin, faint line that terminates at an open circle, is for viscoelastic deformation without plastic failure. The second, shown by a thick, faint line that terminates in a faint solid circle, includes plastic yielding with $c_{dl} = 0$ (no dilatancy). The third, shown by the thick, dark line that ends in a dark circle, has plastic failure with $c_{dl} = 1$. The rate-independent yield surface $F = 0$ is the black line, and the rate-dependent yield function $\mathcal{F} = 0$ is plotted for each case with dashed lines (assuming $c_{dl} = 1$). In the calculations for this panel, the Kelvin viscosity η^K is assigned a large value to expand the contrast between different scenarios.

The most important feature of Fig. 2(d) is the shift in the yield surface from F to \mathcal{F} with the progression of plastic yielding (solid black line *cf.* dashed coloured lines). This rate-hardening is evident in the shifts of the dashed yield curves to higher shear and more negative (i.e. tensile) effective pressure relative to the black yield surface. This behaviour is due to the Kelvin viscoplasticity, and might be thought of as dissipative sliding on a fault or deformation near a dyke tip.

Dilatancy creates another interesting feature in Fig. 2(d). It is most evident in the case of pure shear. Without dilatancy, the stress trajectory remains at constant effective pressure. With dilatancy, the stress trajectory veers toward a larger effective pressure during plastic flow, creating additional compressive stress in the solid phase. This is consistent with the volume confinement $\mathcal{C} = 0$. A more complex behaviour occurs under mixed-mode deformation. Without dilatancy, the stress evolves with the rate-dependent yield surface to negative effective pressures. This tendency is mitigated by dilatancy, which partially accommodates the imposed $\mathcal{C} > 0$. Comparison of these mixed-mode curves demonstrates that the transient peak in τ_{II} is not due to dilatancy, but rather to the differential response to shear and decompaction.

3 COMPUTATIONAL MODELLING OF A TWO-PHASE FLOW

Theory for a poro-viscous two-phase flow is well established and has been analysed in a variety of geodynamic contexts (for a summary and references see Katz 2022; Katz *et al.* 2022). Here we

Table 1. Dimensional parameters for the ODE analysis.

Parameter	Name	Unit	Value
η^K	Kelvin viscosity	Pa s	10^{22}
η_ϕ	Shear viscosity	Pa s	4×10^{22}
ζ_ϕ	Compaction viscosity	Pa s	2×10^{22}
G_ϕ	Shear elastic modulus	GPa	50
Z_ϕ	Compaction elastic modulus	GPa	25
P^l	Liquid pressure	MPa	35
C	Cohesion	MPa	50
θ	Friction angle	°	30
σ_t	Tensile strength	MPa	$12.5 (\sigma_t = C/4)$
ϕ	Porosity	-	0 (shear), 0.5 (compaction, mixed mode)
c_{dl}	Dilatancy coefficient	-	0 (shear), 1 (compaction, mixed mode)
\dot{E}_{II}	Background strain rate	s ⁻¹	10^{-15}

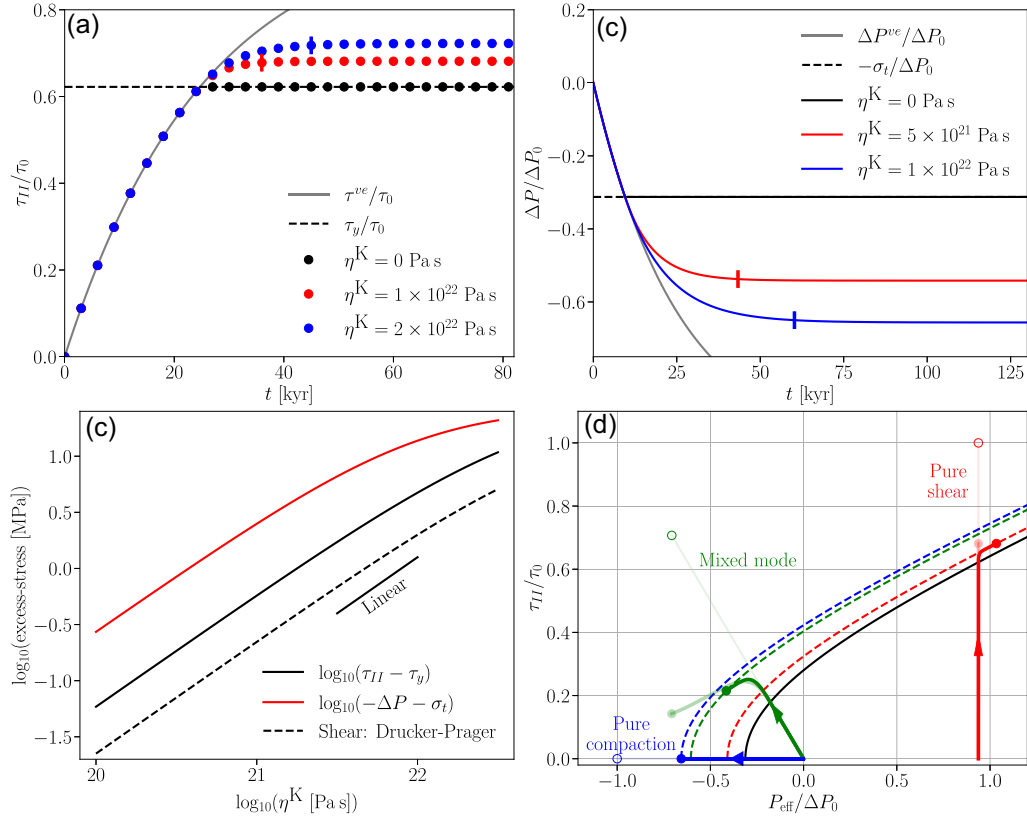


Figure 2. Point-wise stress evolution with a poro-VEVP rheological model according to eqs (18) and (19). (a) Evolution of shear stress in a pure-shear flow. The stresses are rescaled with respect to the long-term viscous stress τ_0 . Numerical results are plotted as circular markers for $\eta^K = 0$ Pa s (black), 10^{22} Pa s (red) and 2×10^{22} Pa s (blue). The solid line shows the analytical results assuming a viscoelastic rheological model. The dashed line shows the yield criterion τ_y . The short vertical lines mark the elapsed time of $4\tilde{t}_{\text{Mw}}$ beyond yielding. (b) Evolution of stress in a pure-compaction flow. Stress is rescaled with respect to the long-term viscous stress ΔP_0 . Analytical solutions of the ODEs are plotted in black, red and blue curves for $\eta^K = 0$, 5×10^{21} and 10^{22} Pa s respectively. The grey line, dashed line and short vertical lines have the same meaning as in panel (a). (c) The variation of excess stress with η^K for the pure shear (black solid) and decompaction flows (red solid). The black dashed lines show the results of the pure shear case but using the Drucker–Prager asymptote of yield function. (d) Trajectories of the stress state with increasing time for: pure-shear flow (red), pure-compaction flow (blue) and mixed mode (green). Arrows indicate the direction of time. P_{eff} and τ_{II} are rescaled according to ΔP_0 and τ_0 , respectively. The dark, medium and faint lines represent configurations with $c_{dl} = 1$, $c_{dl} = 0$, and for a viscoelastic flow, respectively. The circular markers at the end of each curve represent the corresponding steady-state values. Dashed curves correspond to $\mathcal{F} = 0$ at the steady state when $c_{dl} = 1$. The black curve corresponds to $F = 0$.

consider a rheological model that also includes elasticity and plasticity, which complicates the relationship between stress and strain rate. Nonetheless, it is possible to write this physically enriched system in terms of the same Stokes–Darcy system of conservation equations as apply for poro-viscous flow,

$$-\nabla P^l + \nabla \cdot (2\eta_{\text{eff}}\dot{\mathbf{e}}') + \nabla(\zeta_{\text{eff}}C') + \bar{\rho}\mathbf{g} = \mathbf{0}, \quad (24)$$

$$\nabla \cdot \mathbf{v}^s - \nabla \cdot [M_\phi(\nabla P^l - \rho^l \mathbf{g})] = 0, \quad (25)$$

$$\frac{\partial(1-\phi)}{\partial t} + \nabla \cdot (1-\phi)\mathbf{v}^s = 0. \quad (26)$$

In these equations, we have made the Boussinesq approximation for each phase and introduced \mathbf{v}^s as the velocity vector of the solid

phase. Other symbols introduced here are the gravitational acceleration \mathbf{g} and $\bar{\rho} = \phi\rho^l + (1 - \phi)\rho^s$, which is the phase-averaged density with ρ^l and ρ^s the densities of the liquid and solid phase, respectively. Fluid mobility M_ϕ is defined as the ratio of permeability to liquid viscosity. The latter is treated as a constant, whereas the former depends on the local volume fraction of the melt ϕ according to the Kozeny–Carman model. We thus write the mobility as

$$M_\phi = M_0\phi^3(1 - \phi)^{-2}, \quad (27)$$

where M_0 is a constant parameter.

Anticipating a full discretization of the governing equations, we follow Keller *et al.* (2013) and others by introducing a discrete time step Δt and defining a modified deviatoric strain rate tensor and compaction rate, respectively, as

$$\begin{aligned} \dot{\boldsymbol{\epsilon}}' &\equiv \frac{1}{2} \left[\left(\nabla \mathbf{v}^s + (\nabla \mathbf{v}^s)^T - \frac{2}{3} (\nabla \cdot \mathbf{v}^s) \mathbf{I} \right) + \frac{(1 - \phi)\boldsymbol{\tau}^o}{G_\phi \Delta t} \right], \\ C' &\equiv \nabla \cdot \mathbf{v}^s - \frac{(1 - \phi)\Delta P^o}{Z_\phi \Delta t}. \end{aligned} \quad (28)$$

These account for the stress history associated with elastic deformation. To this end, they depend on $\boldsymbol{\tau}^o$ and ΔP^o , the relevant stresses from the previous time step in an Eulerian reference frame [distinct from Keller *et al.* (2013), we neglect the Jaumann derivative of the stress].

Crucially, in eq. (24), we condense the rheological model into two coefficients η_{eff} and ζ_{eff} . We refer to each of these as an *effective viscosity* because they relate the modified strain rates $\dot{\boldsymbol{\epsilon}}'$ and C' to the deviatoric and isotropic stresses. However, they represent the full poro-VEVP response by taking values that vary in time and space as determined by a calculation derived from the model in Section 2 (details in Appendix D).

The partial differential eqs (24)–(26) are solved to obtain $\mathbf{v}^s(\mathbf{x})$, $P^l(\mathbf{x})$ and $\phi(\mathbf{x}, t)$. Given this solution at an instant in time, the phase segregation flux between the liquid and the solid can be recovered with a modified Darcy's law,

$$\phi(\mathbf{v}^l - \mathbf{v}^s) = -M_\phi(\nabla P^l - \rho^l \mathbf{g}), \quad (29)$$

where \mathbf{v}^l denotes the velocity of the liquid phase.

In this paper, 2-D simulations are performed using a Cartesian coordinate system given by (x, z) with unit vectors $\hat{\mathbf{e}}_x$ and $\hat{\mathbf{e}}_z$. The direction of $\hat{\mathbf{e}}_z$ is opposite to the direction of gravity, thus $\mathbf{g} = -g\hat{\mathbf{e}}_z$. Furthermore, we decompose pressure P^l into a dynamic component p^l and a topographic load p^{top} ,

$$P^l = p^l + p^{\text{top}}, \quad \text{where } p^{\text{top}} = \rho^s g(z_s - z) \quad (30)$$

and z_s denotes the location of the top surface. When z_s varies with position x , p^{top} depends on the horizontal location as well as the vertical location, reflecting the deformation of the top surface. Thus, the pressure gradient can be written as

$$\nabla P^l = \nabla p^l + \rho^s \mathbf{g} + \frac{\partial p^{\text{top}}}{\partial x} \hat{\mathbf{e}}_x. \quad (31)$$

The non-dimensional form of the governing eqs (24)–(26) with pressure decomposition (eq. 31) is given in Appendix E. We use the non-dimensional form for all the numerical calculations performed in this paper.

For the numerical computations in this section, we use dimensional parameters as in Table 2 unless otherwise stated. Note that where cohesion varies from its reference value, the tensile strength is defined as

$$\sigma_t = C/4. \quad (32)$$

In the limit of zero melt, $\phi \rightarrow 0$, the system (24)–(26) reduces to the system governing an incompressible Stokes flow of the solid phase only. Eq. (25) reduces to the incompressible continuity equation of a single-phase flow when $\phi \rightarrow 0$, because $M_\phi \sim \phi^3$, as in eq. (27). Then $C = \nabla \cdot \mathbf{v}^s \rightarrow 0$ and the gradient of compaction pressure in eq. (24) reduces to zero as well. Hence eq. (24) reduces to the Stokes equation for single-phase flow with $\bar{\rho} = \rho^s$. In the zero-porosity limit, $P^s = P^l$ represents the solid pressure.

3.1 Discretization and computation

We obtain discrete solutions to eqs (24) and (25) using a staggered-grid, finite-difference spatial discretization (Katz *et al.* 2007; Gerya 2019) with a Newton-type non-linear solver. We demonstrate in Appendix G how solvability under our VEVF formulation can be assured by control of the time step size, despite known convergence issues associated with viscoplasticity (e.g. Spiegelman *et al.* 2016). eq. (26) is discretized in time using the Crank–Nicolson semi-implicit method; the flux divergence is discretized using the Fromm scheme, a second-order upwind finite-volume method (Fromm 1968).

Our results are obtained using the software FD-PDE (Pusok *et al.* 2022a, b) defined by eqs (24)–(26). FD-PDE is built on top of PETSc (Balay *et al.* 1997, 2022b, a), which provides the necessary tools for composing and solving discrete linear and non-linear systems, as well as providing a staggered grid mesh object (DMStag, Sanan *et al.* 2022) that manages fields on the cell faces. The integration of the poro-VEVP framework within FD-PDE is discussed in Appendix H.

For the numerical solutions presented in this paper, the conservation of momentum in the solid and liquid phase and the evolution of porosity are treated as a one-way coupled system; at each time step, \mathbf{v}^s and P^l are obtained by solving eqs (24) and (25) assuming ϕ is fixed, then ϕ is updated according to the velocity field according to eq. (26), assuming that \mathbf{v}^s is constant. At each Newton iteration for solving the momentum equation, the effective viscosity is updated in a manner explained in Appendix D. Note that discretization of the advection term in eq. (26) can result in numerical solutions that exhibit a porosity undershoot, for example $\phi < 0$. The magnitude of this undershoot is less than 10^{-5} if the propagation of a plastic-failure region is well resolved in time. However, even such small negative porosity values can cause solver non-convergence. To circumvent this, after each temporal update of the porosity field we apply the limiter $\phi \leftarrow \max(\phi, 10^{-12})$ cell-wise over the domain. Numerically lagging ϕ in solving for \mathbf{v}^s and P^l reduces the overall computational cost; we validate the accuracy of this approach by demonstrating convergence of results with decreasing time step size in Section 3.2.2.

3.2 Idealized-model results

Here we present numerical results of two idealized models. Section 3.2.1 investigates plastic shear failure and demonstrates the regularizing capability of Kelvin viscoplasticity. Section 3.2.2 investigates plastic tensile failure and demonstrates that it is also regularized by Kelvin viscoplasticity. Moreover, Section 3.2.3 highlights the similarity of the stress field around the viscoplastic region to that predicted by linear elastic fracture mechanics around a fluid-driven fracture.

It is important to note that our smooth yield surface (Fig. 1) does not induce a formal distinction between shear failure and tensile

Table 2. Dimensional parameters for computational modelling.

Parameter	Name	Unit	Value
ρ^s	Solid density	kg m^{-3}	3000
ρ^l	Melt density	kg m^{-3}	2500
η_0	Background shear viscosity	Pa s	10^{23}
G_0	Reference shear modulus	GPa	50
Z_0	Prefactor for bulk modulus	GPa	5
Z_{\max}	Maximum bulk modulus	GPa	100
C	Cohesion	MPa	50
θ	Friction angle	$^\circ$	30
σ_t	Tensile strength	MPa	$12.5 (\sigma_t = C/4)$
M_0	Permeability prefactor	$\text{m}^2 (\text{Pa s})^{-1}$	10^{-9}
g	Gravity constant	m s^{-2}	9.8
$\dot{\epsilon}_{bg}$	Background strain rate	s^{-1}	10^{-15}

failure. In this context, we define shear failure as viscoplastic yielding at positive plastic-effective pressure. Yielding at negative P_{eff} is thus considered to be tensile failure.

3.2.1 Shear failure

To highlight the character and convergence of plastic shear failure under our rheological model, we consider the following simplified setup. The domain is rectangular with dimensions 4×2.8 km and contains solid rock with uniform shear viscosity and shear modulus. The gravitational body force in eqs (24) and (25) is neglected. Boundary conditions impose velocity components associated with a pure-shear flow, extending in the x -direction. The initial condition has zero stress and zero porosity, except that the porosity is set to $\phi = 0.5$ in a semi-circular region with radius 80 m at the bottom-centre of the domain. This locally reduces the viscosity and serves as a ‘weak seed’ for the development of shear failure. Although the stresses in the model evolve with time, the porosity field is held fixed at its initial condition. The time step in this section is $\Delta t \approx 4 \times 10^{-4} t_{\text{Mw}}$.

Fig. 3 presents the results of numerical models with this configuration, plotted at a non-dimensional time of $t/t_{\text{Mw}} \approx 0.05$. Panels (a) and (b) show the logarithm of the strain rate intensity for two values of η^K (other parameters are as in Table 2). Shear bands emanate from the weak seed. For larger η^K in panel (a), the shear bands are diffuse and the background strain rate is lower. At the lower η^K of panel (b), the bands are narrow with sharp edges. This comparison demonstrates the key role of Kelvin viscosity in our models.

The angle of the shear bands in Fig. 3 is independent of η^K . We determine this angle according to the line connecting (0,0) to a point at $z = 1$ km and the value of x with the highest strain rate intensity. These lines form an angle of 58° to the horizontal. This angle falls between the Coulomb angle and the Arthur angle, as expected (Kaus 2010). This demonstrates that our viscoelastic–viscoplastic rheological model gives rise to plastic failure that is quantitatively consistent with previous work.

Panels (c) and (d) of Fig. 3 compare the strain rate intensity along horizontal cross sections at $z = 0.5, 1$ and 1.5 km for models with different spatial resolutions. The curves demonstrate that the width of the shear bands is independent of the grid spacing. They suggest that the peak strain rate intensity converges to a finite value with increasing spatial resolution. These results show that the Kelvin viscosity regularizes the plastic shear bands in our models.

3.2.2 Tensile failure

To highlight the character of plastic tensile failure under our rheological model and the full formulation of two-phase flow (eqs 24–26), the computational problem is configured as follows. The domain is rectangular with dimension 4×2.4 km and contains partially molten rock with viscosities and elastic moduli calculated according to eqs (16) and (17). The boundary conditions impose vertically uniform extension in the x -direction, zero stress at the top, and zero flux of the solid phase at the bottom. The dynamic pressure is fixed to zero at the bottom. The initial condition has zero stress and zero porosity, except for an imposed melt source-region at the bottom. This source has $\phi = 0.2$ at its centre and a Gaussian profile with radial distance. To increase plastic-effective pressure, suppress near-surface shear failure, and hence isolate tensile failure, a 250 MPa static pressure is applied on the top surface. We use a numerical grid of 201×120 cells and set the time step size to $\Delta t = 10$ yr (except where otherwise specified). Later in this section, we examine the numerical accuracy associated with these choices.

Fig. 4 presents the results of a representative numerical solution with this configuration, plotted at a non-dimensional time of $t/t_{\text{Mw}} \approx 0.24$. All panels show a thin, vertical channel that has grown upward from the initially imposed magma source. As we demonstrate below, the features of this channel are closely related to those of a dyke. Although this feature is, at best, a continuum representation of a dyke, we refer to it below as a dyke for concision.

Panel (a) of Fig. 4 shows the porosity distribution. Within the dyke, porosity decays gradually upward from the melt source. Horizontally across it, the porosity changes abruptly from zero to a finite value and back to zero. Defining the melt-bearing region as $\phi > 10^{-4}$, we find that it has a maximum height at this time of $z_t = 1.65$ km, while its width is about 40 m.

Panels (b) and (c) of Fig. 4 show the logarithm of the shear-strain rate and the decompaction rate, respectively. Both are elevated by up to three orders of magnitude inside the dyke. The maximum value of $\nabla \cdot \mathbf{v}^s$ is $\sim 10^{-12} \text{ s}^{-1}$ which applies close to the tip at $z = 1.63$ km where $\phi = 0.001$. This large decompaction rate, much larger than the background strain rate, is associated with plastic failure and rapid propagation of the dyke tip. The vector plot in this panel shows the velocity field of the solid phase. Evidently, there is a near-discontinuous change across the dyke. This is a feature associated with plastic failure that would not occur in a viscoelastic flow.

Panels (d)–(f) of Fig. 4 show the shear stress, the decompaction stress, and the overstress, respectively. The latter is the consequence

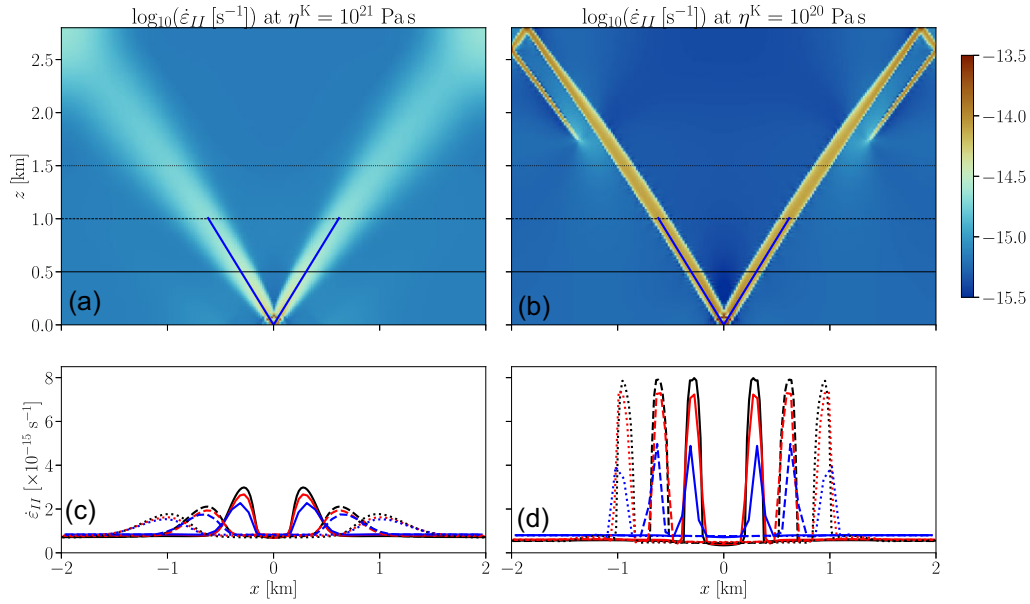


Figure 3. Shear failure for $\eta^K = 10^{21}$ Pa s (left-hand panel) and 10^{20} Pa s (right-hand panel) at $t = 3$ kyr. Other parameters are shown in Table 2. Panels (a) and (b) show the intensity of shear-strain rates for $\eta^K = 10^{21}$ and 10^{20} Pa s, respectively, with a grid size of 201×140 cells. The blue lines highlight the orientation of shear bands. Panels (c) and (d) show profiles of $\dot{\epsilon}_{II}$ along three horizontal slices at $z = 0.5$ km (solid lines), 1 km (dashed lines) and 1.5 km (dotted lines) for grids with cell numbers given by 201×140 (black), 101×70 (red) and 51×35 (blue). The corresponding slices have been highlighted in panels (a) and (b) using the same line styles.

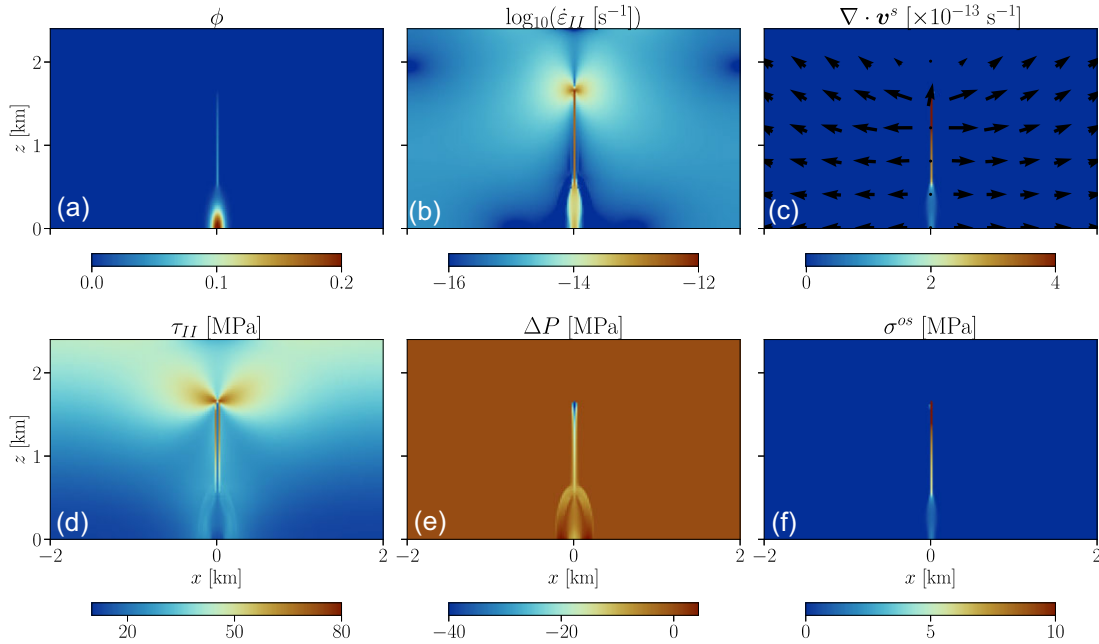


Figure 4. Snapshots showing the tensile failure when $\eta^K = 10^{19}$ Pa s at $t = 15$ kyr. The initial melt follows a Gaussian distribution centred at (0 km, 0 km) with $\phi = 0.2$ which has the decay lengths of 80 and 240 m in the x and z direction, respectively. Other physical parameters are shown in Table 2. The grid contains 201×120 cells. The size of the time step is $\Delta t = 10$ yr. These snapshots include (a) porosity, (b) deviatoric strain rate, (c) isotropic strain rates, (d) shear stress, (e) decompaction stress and (f) overstress (eq. 33). The vector field in the panel (e) represents the solid velocity. The colourscale in panel (c) is truncated to provide contrast along the dyke below its tip.

of introducing the Kelvin viscosity and is defined as

$$\sigma^{os} = \eta^K \dot{\lambda}. \quad (33)$$

Panel (d) shows relatively low shear stresses along the centre of the dyke and high shear stresses around the outside of the tip. Panel (e)

highlights the overpressure of the liquid phase along the channel, indicated by the negative value of ΔP , which is especially strong near the tip. It implies a concentration of tensile stress at the dyke tip that promotes fracture, and a sufficient tensile stress along the dyke to maintain its opening. Correspondingly, panel (f) highlights

that the whole channel is subject to plastic failure, but the tip is the locus of the strongest plastic deformation. Each of these results demonstrate that the region of tensile plastic failure that we refer to as a dyke has the characteristics of a fluid-filled fracture.

Fig. 5 overlays numerical results obtained with different values of the Kelvin viscosity, $\eta^K = 10^{19}$, 10^{20} and 10^{21} Pa s. Panel (a) compares the outline of the dyke, defined as the region where $\phi \geq 10^{-4}$. Consistent with results for plastic shear failure (Fig. 3), the dyke is thinner for smaller η^K . The width of the dyke when $\eta^K = 10^{19}$ Pa s is $\sim 1/6$ of the value when $\eta^K = 10^{21}$ Pa s. Panels (b)–(e) of Fig. 5 compare a selection of variables along a vertical section at $x = 0$ km, from the bottom boundary to the tip of the melt channel. This section is highlighted in panel (a) as a dotted line. Panel (b) shows the logarithm of the decompaction rate for the three cases. The decompaction rate $\nabla \cdot \mathbf{v}^s$ is approximately one order of magnitude larger for $\eta^K = 10^{19}$ Pa s than for $\eta^K = 10^{21}$ Pa s. The higher decompaction rate at the dyke tip indicates a faster propagation rate for a smaller η^K . Panels (c)–(e) compare shear stress, decompaction stress and overstress for these three cases, respectively. The plots are consistent with our observations in panels (d)–(e) of Fig. 4. Comparing the results at different η^K shows that the magnitudes of ΔP and σ^{os} are higher for larger η^K along the entire channel, but the shear stress intensity τ_{II} shows little difference between the three curves, except in the tip region of the dyke. These observations imply that the liquid overpressure, not shear, dominates the plastic failure and also increases with increasing η^K .

Panel (f) of Fig. 5 compares the vertical propagation rate of the dyke tip for different η^K . Evidently, the tip propagates faster with a smaller value of η^K . When η^K is reduced by $100 \times$ from 10^{21} Pa s, the propagation rate is $\sim 10 \times$ faster. This plot indicates that the Kelvin viscosity, by regularizing tensile failure, also regularizes the rate of dyke-tip propagation.

Fig. 6 explores the effects of resolution and parameter differences on dyke width and propagation rate. Panels (a)–(c) confirm that numerical results at the default grid of 201×120 cells are nearly converged by comparing them with three other grids consisting of 51×30 , 101×60 and 401×240 cells. Panels (a)–(b) show the deviatoric and isotropic strain rates along a narrow horizontal cross section at $z = 1.2$ km. The comparison shows that the width of plastic failure and the maximum strain rate are independent of grid spacing for grids of 201×120 cells or larger. Panel (c) compares the propagation of the dyke tip between the four grids. This comparison confirms that the grid with 201×120 cells can provide a nearly converged solution. Therefore, panels (a)–(c) together demonstrate that mesh-independent results for tensile failure in an appropriately regularized two-phase model are achievable with adequately fine resolution.

Panel (d) of Fig. 6 shows three sensitivity tests on the propagation rate of the dyke tip. This rate is calculated as the average speed of the tip travelling from $z = 1.2$ to 2.2 km. The grey, square markers compare the propagation rate for four different sizes of time step, $\Delta t = 50, 25, 10$ and 5 yr. The successive differences between rates for each refinement confirm that numerical convergence, in terms of the temporal step size, is achieved. The default choice $\Delta t = 10$ yr balances convergence with computational cost; reducing Δt by 50 per cent creates a ~ 3 per cent increase in propagation rate. Secondly, this panel shows the dependence of propagation rate on the imposed extensional rate (red line) and magmatic buoyancy (black line). Evidently, it is the extensional force that dominates the propagation of the tensile failure; increasing the buoyancy only leads to a slight increase in the propagation rate.

Taken together, the results of this section support the hypothesis that tensile plastic failure in a two-phase, V EVP model is a continuum mechanical representation of the physics of dyking. They also extend the regularizing properties of the Kelvin-viscoplastic rheological unit (Borst & Duretz 2020). With the reduction of η^K , the continuum representation of a dyke becomes thinner and propagates faster—that is, it behaves more like a natural dyke. However, this convergence incurs a sharply increasing computational cost because smaller grid sizes and time steps are required to resolve the solution. In the next section, we validate our formulation and further test its relevance by comparing it with the linear elastic fracture mechanics model for the discrete analysis of dyking.

3.2.3 Comparison with linear elastic fracture mechanics

Fluid-filled fractures including dykes are typically modelled as discrete inclusions in an extended continuum. The walls of the dyke are boundaries where the flow solution within the dyke is matched to the (visco)elastic solution outside of it (Detournay 2016). Conditions at the fracture tip determine whether the tip propagates, and at what speed (Detournay 2016). Our continuum model excludes all of these details. And yet it exhibits dyke-like behaviour: a slender, gravity-aligned zone of mechanical weakness with a clearly defined, propagating tip. In this section, we aim to show that the stress distribution at the upper tip of the continuum representation of a dyke matches that of an idealized, mode-I fracture in an elastic medium.

To quantify the similarity with linear elastic fracture mechanics (LEFM) we compare the full stress field σ from the poro-V EVP model (Fig. 4) with LEFM solutions for stress distribution at the tip of a fluid-filled fracture. From LEFM theory, the stress distribution at the tip of an opening-mode fracture (mode-I) is approximated by

$$\begin{Bmatrix} \sigma_{xx} \\ \sigma_{zz} \\ \sigma_{xz} \end{Bmatrix} = \frac{K_I}{\sqrt{2\pi r}} \begin{Bmatrix} \cos(\vartheta/2)[1 - \sin(\vartheta/2)\sin(3\vartheta/2)] \\ \cos(\vartheta/2)[1 + \sin(\vartheta/2)\sin(3\vartheta/2)] \\ \sin(\vartheta/2)\cos(\vartheta/2)\cos(3\vartheta/2) \end{Bmatrix}, \quad (34)$$

where K_I is the mode-I stress intensity factor; Fig. 7(a) shows the crack-tip r, ϑ polar coordinate system. Eq. (34) comprises two factors: the asymptotic near-tip stresses as a function of angle ϑ and their dependence on distance r from the fracture tip. For all three components of the stress tensor, stress increases with $r^{-1/2}$ as $r \rightarrow 0$. Terms within the curly brackets describe how the stress varies with the angle around the tip.

To facilitate a comparison with stresses predicted by eq. (34), we must make a choice regarding the precise location of the fracture tip in a numerical solution of the V EVP model. We take this as the centre of the highest grid cell in the model where there is liquid overpressure, that is where $\Delta P < 0$ (Fig. 7a).

It is unclear how to analytically relate the LEFM critical stress intensity factor K_I to the structure of the plastic yield curve. Therefore, to compare the V EVP solution with eq. (34), K_I is adjusted to provide the best fit to the magnitude of the σ_{xz} component of stress in the V EVP model; we retrieve $K_I = 1.5 \text{ GPa m}^{1/2}$. Fig. 7(b) then shows a comparison of σ_{xz} between the LEFM and V EVP models as a function of ϑ . Except at certain angles that fall within the plastic-failure zone behind the dyke tip, the correspondence is remarkable.

A similarly good fit is obtained for the normal stresses, though this is achieved by subtracting a uniform offset from the numerical solution. This offset is a consequence of the background, far-field stress arising from the imposed extension, the lithostatic stress, and the additional static stress imposed to suppress shear failure in this

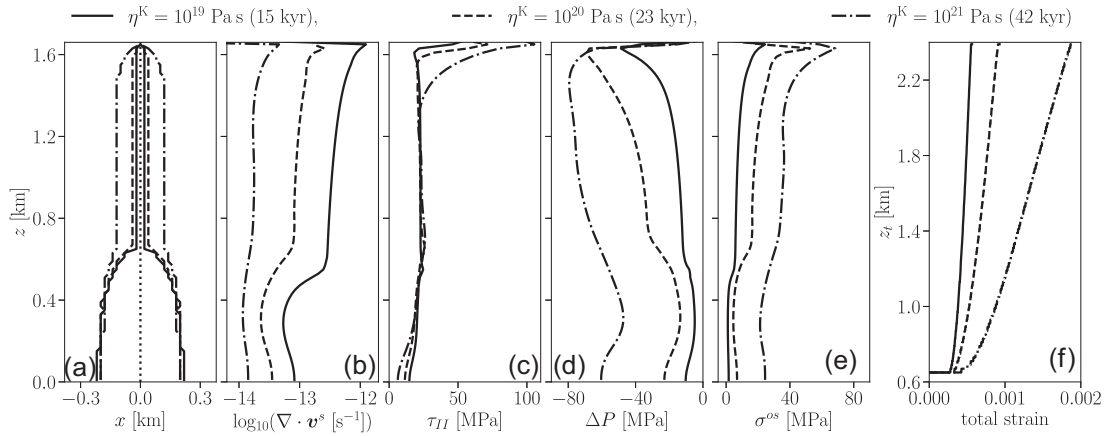


Figure 5. Comparison of dyke characteristics for $\eta^K = 10^{19}$ Pa s (solid line), 10^{20} Pa s (dashed line) and 10^{21} Pa s (dashed-dotted line). The dyke propagation rate differs in each case and hence, to compare the structure at equal dyke heights ($z_t = 1.65$ km), the results are extracted at model times of 15, 23 and 42 kyr, respectively. All cases have $\Delta t = 10$ yr and a grid of 201×120 cells. Panels (a)–(e) show the snapshots that all three cases have the same height of the melt channel as shown in Fig. 4, which includes the profiles of the melt channel where $\phi > 10^{-4}$ (a) and the profiles of several physical variables along $x = 0$: the size of decompaction rate (b), the magnitude of the shear (c) and decompaction stress (d) and the overstress (e). Panel (f) shows the tip location z_t of the channel versus the total strain of this whole domain.

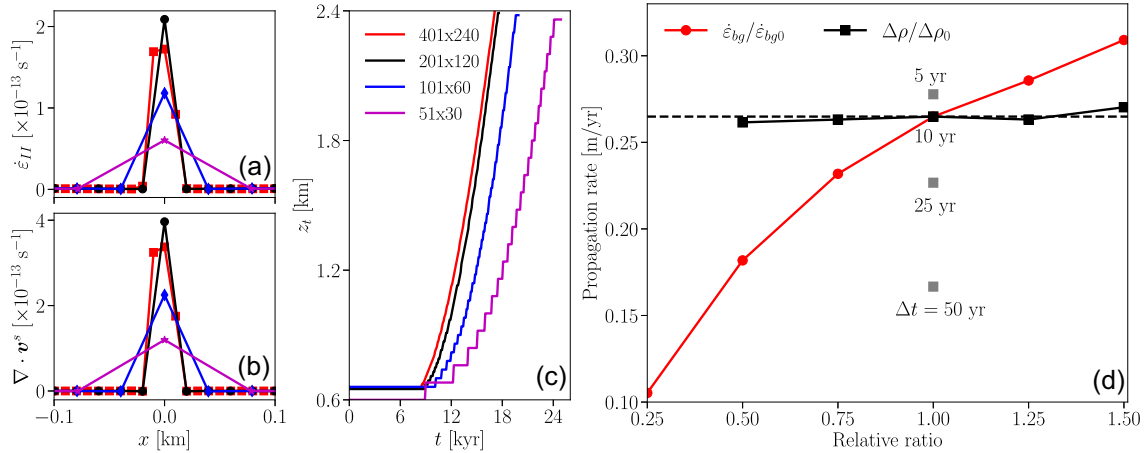


Figure 6. Sensitivity of the numerical solution to spatial and temporal resolution and parameter values. Panels (a) and (b) show a narrow horizontal cross-section at $z = 1.2$ km across the dyke for the deviatoric and isotropic strain rates respectively. Line colours indicate grid dimensions according to the legend in panel (c). The model time for each curve is $t = 21, 17, 15$ and 15 kyr, respectively, such that the dyke has the same height in all cases. Markers correspond to values at grid points. (c) The tip location z_t versus time t for the four grid sizes. (d) The propagation rate of the dyke tip at different time step sizes (grey squares), extension rates (red circles) and magmatic buoyancy (black squares). Each marker represents a different simulation result. The propagation rate is calculated as the average speed of the tip between $z = 1.2$ and 2.2 km. $\Delta\rho_0$ and $\dot{\epsilon}_{bg0}$ are the values for the reference case of Table 2 and Fig. 4. The dashed line shows the propagation rate of the reference case.

case. All three stress components match the angular distribution predicted by LEFM in both magnitude and form (except within the plastic-failure zone).

Moreover, panel (c) of Fig. 7 shows a comparison with the radial distribution of stress from eq. (34). Stress components should vary with the distance from the tip as $r^{-1/2}$. In Fig. 7(c), the VEP and LEFM values of σ_{xx} and σ_{zz} at $\vartheta = 0$ are compared. Sufficiently far below the free surface (its position is indicated by the dotted–dashed line) and close to the dyke tip, the poro-VEVP results have the same asymptotic form to the LEFM model.

The remarkable correspondence between these independent approaches further supports the hypothesis that two-phase, poro-VEVP tensile failure is a continuum mechanical representation of dyking. However, a comparison of liquid pressure and its vertical

gradient highlights a key difference: that the continuum representation is a porous channel rather than an open fracture. This accounts for the much slower ascent speed of the poro-VEVP dyke. In the next section, we address this discrepancy.

3.3 Geodynamic-model results

In the previous section, idealized models were used to document a quantitative similarity with the standard, LEFM model of dykes. Here we use a model at lithospheric scale to develop preliminary predictions for magma-assisted tectonics. We consider a simplified but geodynamically relevant configuration to highlight the role of magmatic dykes in rifting. The domain is a square with sides of 100 km. Initially, a layer of sticky air fills the top 20 km of the

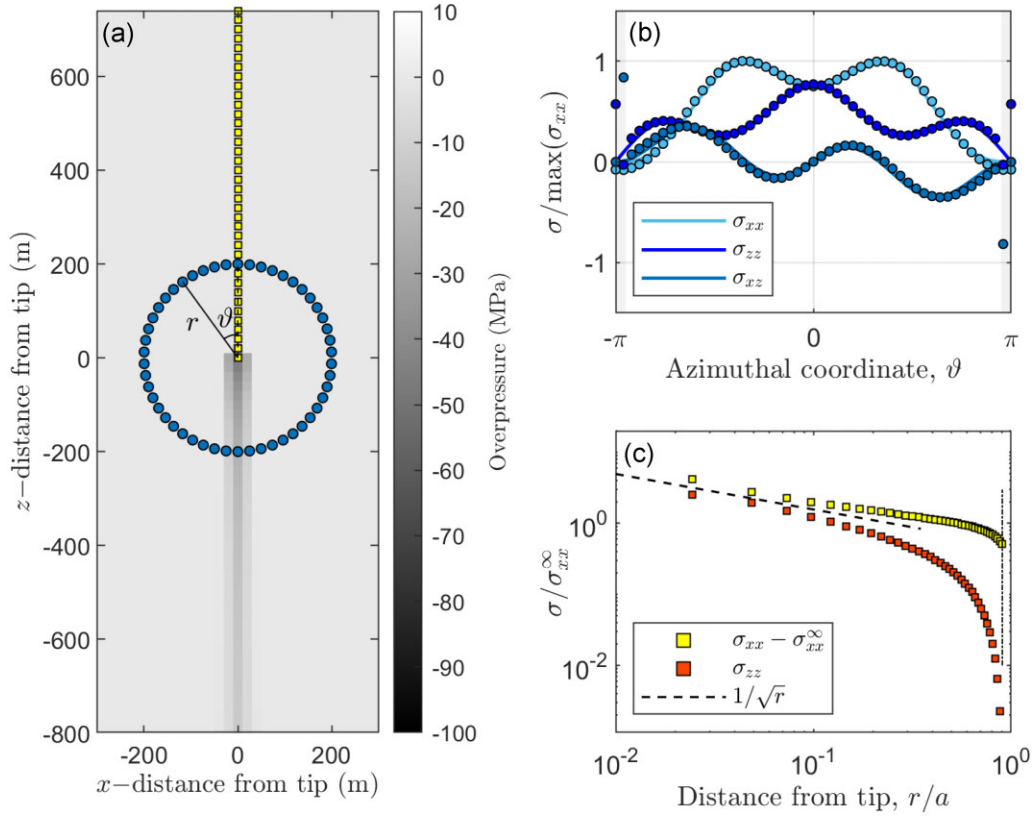


Figure 7. Comparison of LEFM and poro-VEVP models the normalized stress distribution around a dyke tip. (a) Fracture-tip coordinate system with angle ϑ measured counter-clockwise away from vertical and radial distance r from the origin. The poro-VEVP results on the background grid are shaded by liquid overpressure (ΔP). (b) Fracture-tip stress distribution. The LEFM solutions (34) are shown as solid lines and stresses from the VEP solution are shown as points. VEP stress components have been interpolated onto a ring of points, evenly spaced in ϑ around the fracture at $r = 200$ m. These points are shown in panel (a) as blue dots. Regions where $|\vartheta| > 19\pi/20$ are shaded grey. (c) Fracture-tip stress asymptote. Squares show the VEP results ahead of the fracture tip along $\vartheta = 0$; the location of these points are shown in yellow in panel (a). The dashed line is the LEFM $1/\sqrt{r}$ singularity from eq. (34). We approximate the horizontal stress (σ_{xx}^∞) at this time as 42 MPa by assuming a Maxwell viscoelastic response to the imposed extension. The position of the free surface in the VEP model is shown by a vertical dashed-dotted line.

domain while the bottom 80 km is filled by rock. We parametrized a slender magma chamber by defining an initial porosity that follows a Gaussian distribution which has $\phi = 0.5$ at (0 km, 25 km) and a decay length of 2 and 6 km in the x and z directions, respectively. The reference shear viscosity is parametrized with height in the domain as $\eta_0(x, z) = 10^{20+z/(20 \text{ km})}$ Pa s such that $\eta_0 = 10^{20}$ Pa s at the bottom and $\eta_0 = 10^{24}$ Pa s at the initial free surface. The reference shear modulus and bulk moduli are taken as constants. The rheological model of eqs (16) and (17) is used to incorporate the porosity dependence into these rheological coefficients. We choose boundary conditions to impose a vertically uniform rate of extension in the x direction associated with a nominal background strain rate $\dot{\epsilon}_{bg}$. There is no slip of the solid on the left and right, and zero traction on the solid at the top and bottom boundaries. We use a numerical grid consisting of 201×200 cells and an initial time step size of $\Delta t = 100$ yr. The time step is reduced to $\Delta t = 20$ yr as needed to achieve convergence of the Newton solver.

We use the phase-field method to track motion of the interface between sticky air and rock. This method has been proven effective for solving free-surface problems in engineering (Sun & Beckermann 2007; Chiu & Lin 2011; Mirjalili *et al.* 2019, Mirjalili *et al.* 2020; Mirjalili & Mani 2020). We modify the method to capture subgrid-scale topographic displacements. The theory and our modifications are summarized in Appendix F.

To improve the geodynamic relevance of the model, three modifications are made to the configuration. First, a random perturbation is applied cell-wise to the cohesion in the range $\delta_C \in [-5\%, 5\%]$ of the reference cohesion $C_0 = 50$ MPa. This represents heterogeneity of rock competence. Secondly, plastic-strain softening is introduced with the linear relation,

$$C = C_0(1 + \delta_C) \left[1 - \frac{1}{2} \min \left(\frac{\lambda}{\lambda^*}, 1 \right) \right], \quad \text{where } \lambda = \int_0^t \dot{\lambda} dt, \quad (35)$$

where λ represents the accumulated plastic strain. $\lambda^* = 0.01$ is a scale chosen to achieve a softening effect similar to that of fig. 1(b) in Duretz *et al.* (2021). The minimum value in the bracket on the right-hand side of the equation means that the maximum relative reduction of cohesion is 50 per cent. Tensile strength σ_t varies with cohesion as in eq. (32). Finally, we introduce an enhancement of permeability arising from plastic strain. This is achieved by modifying the Kozeny–Carman relation to read

$$M_\phi = M_0 \phi^3 (1 - \phi)^{-2} \{1 + \kappa [1 - \exp(-\lambda/\lambda^*)]\}, \quad (36)$$

where κ is an amplification ratio. We take $\kappa = 100$ as a reference value but later investigate the sensitivity of results to this choice.

In the geodynamically inspired models of this section, both shear and tensile failures should occur. Given the background strain rates

and assuming only a viscous rheological response, the shear stress at the free surface is approximately 2000 MPa, whereas at the bottom of the domain is 0.2 MPa. The former is much larger than cohesion at the top surface, where the static pressure is zero. When the plastic limit in eq. (13) is applied, shear failure occurs from the surface downward to a depth where the yield stress τ_y is not exceeded. Moreover, in the presence of a concentrated supply of magma at depth, upward-propagating tensile failure similar to that shown in Section 3.2.2 is expected as well.

These outcomes are illustrated in a snapshot from a simulation in Fig. 8. This figure shows results for the reference-case geodynamic model at $t = 23$ kyr with parameters as given in Table 2. This time is $\approx 0.04t_{\text{Mw}}$ at the free surface and $t/t_{\text{Mw}} \gg 1$ at the bottom of the domain. Colour in panel (a) represents the logarithm of shear viscosity, which illustrates the depth-dependent background viscosity. The oval with low viscosity corresponds to the high-porosity magma chamber. Above it, a thin channel represents a dyke with a maximum porosity of ≈ 0.06 . Vectors in this panel represent the velocity of the solid phase. There is downward flow in a small region above the dyke tip. This motion is associated with proximity of the free surface; it is suppressed in the idealized model of Section 3.2.2.

Panel (b) of Fig. 8 shows the logarithm of accumulated plastic strain λ . There is a strongly strained, vertical band associated with tensile failure, as well as shallow, oblique bands across the free surface arising from shear failure. Similar near-surface bands of plastic-shear failure appear outside of the horizontal range shown in the panel. As discussed above, this accumulated plastic strain can be considered to represent dyking and faulting. In this model, however, there is evidently a mechanical interaction between the dyke and the faults. Shear bands with larger amplitude and deeper penetration form a triangular region above the tip of the dyke. They appear when the dyke tip is sufficiently close to the surface and connect the two. Identical behaviour was noted by Keller *et al.* (2013) and predicted by Rubin & Pollard (1988). Panel (b) also shows that the plastic-strain reduction of cohesion and enhancement of permeability are saturated inside the dyke and at some bands along the surface.

Panels (c) and (d) of Fig. 8 show the second invariants of the shear strain rate and the shear stress, respectively (see Movie S1 for evolution of the $\dot{\epsilon}_{II}$ field and the $\phi = 10^{-4}$ contour). The strain rate field demonstrates that the dyke and its conjugate shear bands are the only instantaneous plastic flow at this time step. The near-surface shear bands appearing in panel (b) are inactive; their plastic strain was accumulated previously. The shear-stress distribution shows that stress is relieved along the walls of the dyke and concentrated ahead of the dyke tip. Indeed it is this stress that promotes deformation in the conjugate faults.

Motivated by an interest in understanding the resistance of the lithosphere to magma-assisted rifting, we consider the yield strength along the pathway of the dyke. Fig. 9(a) shows a profile of τ_y , calculated according to eq. (13), at $x = 0$ km for $t = 0, 19, 21, 23$ and 25 kyr. In computing τ_y , the plastic-effective pressure is evaluated using eq. (7), in which all required values are extracted from the numerical model. The yield strength characterizes the lithospheric resistance in the high-viscosity region, but not in the low-viscosity region, where the resistance is negligible (hence Fig. 9a is only for $z \geq 20$ km). We also neglect the topography (of less than 30 m) that develops over the time range of this plot. This panel indicates that the lithospheric strength decreases with time as a result of the vertical propagation of the dyke tip. For each curve, the dyke tip is located just beneath the height where τ_y rises sharply. Below the tip, within the dyke, the porosity is increased and hence the

plastic-effective pressure of the solid is sharply reduced because $P_{\text{eff}} \approx \Delta P$. Thus, according to eq. (13), τ_y is small within the dyke. Above the tip and upwards, τ_y experiences a maximum value and then gradually decreases to a very small value at the free surface. The maximum value decreases with upward propagation of the tip, whereas the slope of τ_y ahead of the peak value remains roughly constant. To understand this pattern, consider that when the dyke tip is sufficiently deep, τ_y is approximately linear with P_{eff} ; this is the Drucker–Prager limit of the yield function. Where porosity is very small or zero, P_{eff} is dominated by the static pressure and hence the linear increase in τ_y with depth. To summarize Fig. 9(a), magma in the dyke weakens the lithosphere by lowering the plastic-effective pressure (Terzaghi’s principle) within the dyke, which reduces the plastic yield strength and promotes advance of the dyke tip by plastic failure.

Panel (b) of Fig. 9 illustrates the vertical propagation of the dyke tip. Height of the tip is plotted against time for three different values of the plastic-strain enhancement factor κ for permeability. An increase from $\kappa = 1$ to 100 leads to a $\sim 10 \times$ faster propagation rate. Note that κ is a parameter representing somewhat abstracted physics. A natural dyke has zero solid fraction in its interior and a relatively low rate of viscous dissipation as a consequence; in contrast, the continuum representation is wide and porous, leading to Darcy drag and higher viscous dissipation. An increased value of κ reduces the Darcy drag and dissipation, yielding more rapid flow, higher magma pressure at the tip, and faster tip propagation. These bring the behaviour of the continuum representation closer to that of the natural system.

4 DISCUSSION

4.1 Extensional force for magma-assisted rifting

In the sections above, we have developed and analysed a theory for viscoelastic–viscoplastic two-phase flow of partially molten rock at melt fractions below disaggregation. This development was aimed to build on the successes and address the deficiencies of Keller *et al.* (2013) in modelling the effect of magma on lithospheric deformation. The results described in Section 3.2 demonstrate that our theory provides a continuum representation of faults and dykes that allows for their self-consistent emergence and interaction. We have demonstrated regularity and numerical convergence of the discrete solutions and, for certain aspects, convergence of the models to analytical solutions.

These results and their interpretation enable us to give quantitative, mechanistic meaning to the term magma-assisted tectonics (Kendall *et al.* 2005). The aim of doing so was perhaps first articulated by Buck (2004) and Buck (2006), who compared the force required for rifting with or without a magmatic intrusion. The estimates produced by Buck (2006) were based on simple, transparent and analytical calculations. But the models relied on strong assumptions that limit their predictive scope. Our aim in developing the present theory is both to confirm the conclusions of Buck (2006) in a more general context and to create a robust theoretical platform with a broader scope for testable predictions. In the next paragraph we directly address the former aim; progress towards the latter is demonstrated throughout this paper but limitations of the current work are discussed later.

To compare the dynamics of rifting under different model assumptions, we define the extensional force as the force (per distance out of the plane) required to cause lithospheric extension at a given

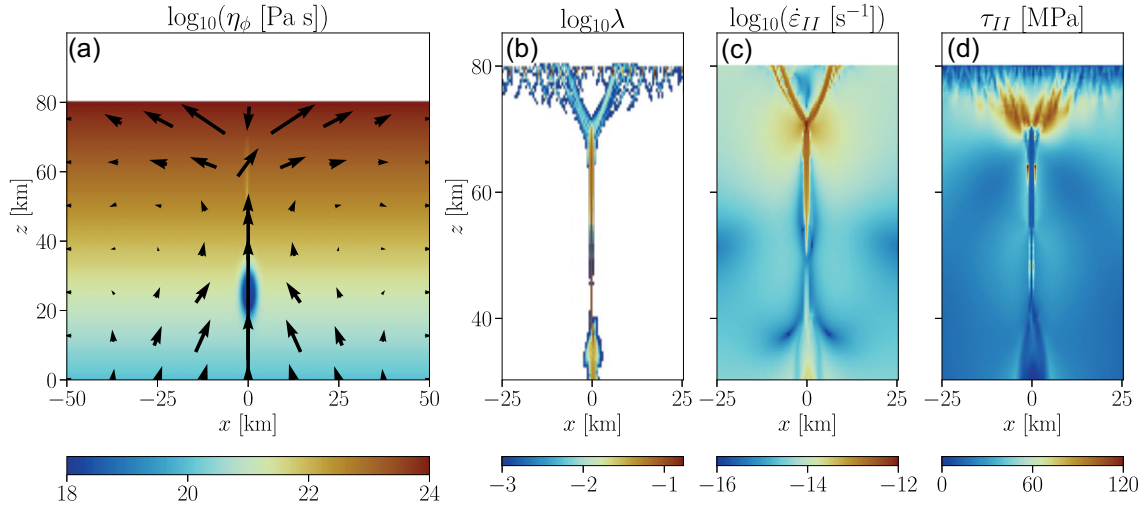


Figure 8. Snapshots of the reference geodynamic model with depth-dependent viscosity $\eta_0 = 10^{20+z/(20\text{ km})}$ Pa s and Kelvin viscosity $\eta^K = 10^{19}$ Pa s at $t = 23$ kyr. Strain softening is applied as in eq. (35). Permeability enhancement is applied as eq. (36) with $\kappa = 100$. Panels show: (a) vectors of the solid velocity and shear viscosity; (b) accumulated plastic damage as defined in eq. (35); (c) second invariant of shear-strain rate and (d) the second invariant of the shear stress. In panels (b)–(d), the domain is truncated to highlight the dyke and the central region of the faults.

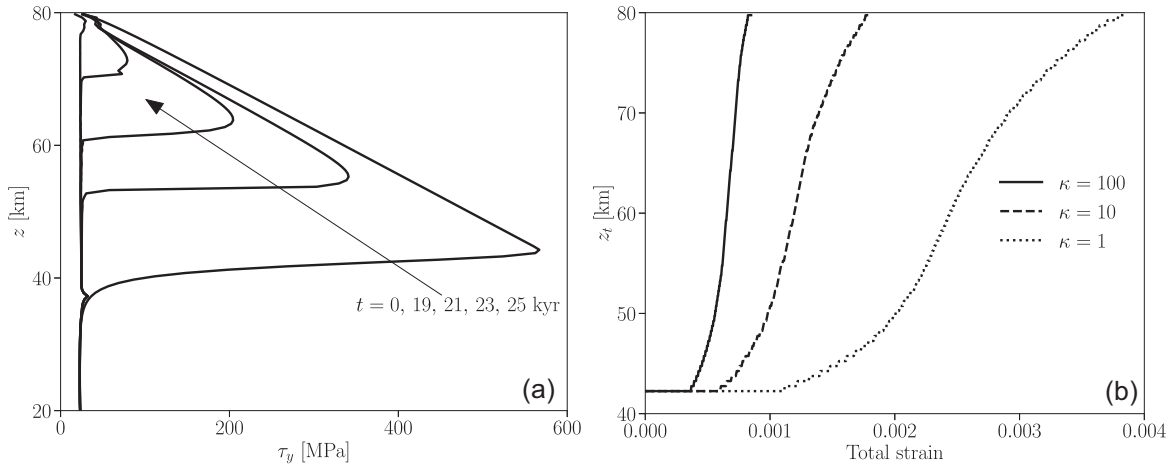


Figure 9. (a) Profiles of the yield strength τ_y along a vertical slice at $x = 0$ km for $t = 0, 19, 21, 23$ and 25 kyr. The arrow indicates the progression of time amongst the curves. Yield strength τ_y is calculated according to eq. (13) using values extracted from the numerical results. (b) The dyke-tip height as a function of the total strain across the domain for three values of the permeability enhancement parameter κ .

rate. This force is calculated by integrating $-P^s + \tau_{xx}$ along the side boundary. Fig. 10 plots the evolution of this extensional force at a rate of 10^{-15} s^{-1} for rifting with and without mechanical participation of magma (also see Movies S1–S3). Results are plotted for a set of scenarios that are modifications of the geodynamic reference model of Section 3.3 and Fig. 8. A purely viscoelastic model without plastic failure is the most basic case; a VEP model without magma (the ‘Tectonic’ curve, $\eta^K = 10^{19}$ Pa s) allows for plastic failure by shear; finally, we consider three poro-VEP models with magmatism and with $\eta^K = 10^{19}, 10^{20}$ and 10^{21} Pa s. The simulations with magmatic rifting are terminated when the dyke reaches the free surface.

All of the curves in Fig. 10 follow the same initial, viscoelastic trajectory. Extensional stress in the lithosphere increases until it causes plastic failure in the cases where this is allowed. The case without plastic failure continues along the viscoelastic trajectory to

a very large force. Cases with the VEP rheological law deviate from this trajectory due to plastic failure, which relieves some of the accumulated stress. As is evident by the comparison between the tectonic curve and the magmatic curves, tensile failure associated with magmatic dykes is much more effective in reducing the maximum extensional stress (and force). This pattern reflects the loss of plastic strength with dyke propagation, as illustrated in Fig. 9(a). Furthermore, the involvement of magmatism leads to a maximum in the force and a subsequent decline.

By comparison of the three magmatic cases of Fig. 10, it is clear that the viscosity η^K of the Kelvin viscoplastic element plays an important role in determining the strength of the lithosphere during and after dyke injection. Based on results shown in Fig. 5(f), it is known that the dyke propagates faster for smaller η^K . Hence the force maxima of Fig. 10 are achieved earlier and are consequently smaller with decreasing η^K . Based on the three values of η^K

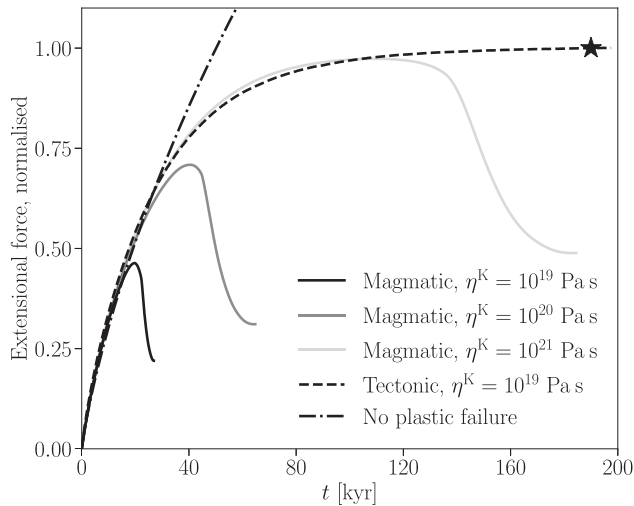


Figure 10. Extension forces for magmatic rifting at $\eta^K = 10^{19}$ Pa s (black line), 10^{20} Pa s (grey line) and 10^{21} Pa s (light grey line) and tectonic rifting at $\eta^K = 10^{19}$ Pa s (dashed line). The calculation for magmatic rifting is terminated once the dyke reaches the free surface. All force values are scaled with respect to 8.2 TN m^{-1} which is the force for tectonic rifting at $t = 190 \text{ kyr}$ (star marker). For comparison, the dotted–dashed line shows the force in the absence of plastic failure. The force is obtained by integrating σ_{xx} vertically along the lateral boundary at $x = 50 \text{ km}$.

considered, it is not clear whether further reduction would lead to convergence to a limiting force trajectory; the computational cost of resolving features at smaller η^K precludes addressing this question here. However, we note that dyke height at the maxima of extension force are similar: 24, 25 and 31 km beneath the free surface for $\eta^K = 10^{19}$, 10^{20} and 10^{21} Pa s, respectively.

These force predictions, although preliminary, are consistent with the broad conclusions of Buck (2006). The presence of magma and, in particular, the mechanics of magmatic dykes enable extension of lithosphere at a much reduced extensional force than in its absence. In Fig. 10, magmatic rifting occurs at a force that is between 20 and 50 per cent of tectonic rifting at $\eta^K = 10^{19}$ Pa s.

While there is broad agreement with the conclusions of Buck (2006), there are significant points where the models differ from each other or from the natural system. Most obviously, we include a viscous resistance to plastic failure whereas in Buck (2006), there is no inherent strength across the dyke. Moreover, in Buck (2006), a dyke exists as a fully formed magmatic conduit and is analysed in terms of its instantaneous effect, whereas our dyke evolves on a timescale that is resolved by the simulation. The real situation is more complex in many ways, of course, but especially in that dykes solidify over days to years, depending on their thickness, and may be repeatedly injected in close proximity (e.g. Bolchover & Lister 1999; Rivalta *et al.* 2015). Hence their tectonic effect is neither steady, as implied in Buck (2006), nor slowly evolving in the way predicted here. This also has implications for the role of extensional stress: for Buck (2006) it balances the tendency of the dyke to empty and close whereas here it serves to promote propagation of the tip. Moreover, neither study considers the cumulative thermal impact of dyke injections; this was accounted for by Bialas *et al.* (2010). In light of these and other differences, it is perhaps most interesting that independent investigations of the same question with entirely distinct formulations are in agreement on the answer to that question.

4.2 Model limitations

Our aim in this paper was to develop a continuum theory capable of describing melt transport through the poro-viscous asthenosphere and the elastic–brittle lithosphere. In particular, we sought a continuum representation of dyking—the propagation of magma-filled fractures. We have demonstrated above that the behaviour of numerical solutions to our theory is, in some ways, quantitatively similar with LEFM models of dykes as discrete fractures. Although promising, there are various limitations of our model in its current state. We discuss several here, noting that some of these may be mitigated or overcome through further development and analysis.

Most fundamentally, natural dykes are discrete discontinuities (fluid-filled fractures) in a continuous medium (the host rock). They create and expand a sharp interface between solid rock and liquid magma. Both the benefit and drawback of a continuum approach to modelling dykes is that it replaces the narrow, discrete fracture with a distributed zone of plastic failure. By viscous regularization, this zone is resolved over several grid cells at minimum; a width that may be substantially larger than that of its discontinuous, natural counterpart. And whereas the ‘porosity’ inside a natural dyke is unity, in the continuous representation the porosity is much lower. Indeed we might expect it to scale as the width ratio of the natural dyke to its continuum representation, though other controls are certainly relevant. The porosity ϕ of continuum dykes sets their permeability and hence the viscous drag on the liquid; in LEFM models, the drag is modelled in terms of a Poiseuille flow in the narrow gap between fracture walls. It seems obvious that this difference has implications for the pressure drop along the dyke, the viscous dissipation, and the tip-propagation speed (see Fig. 6d), though these are not straightforward to calculate. It may be possible to calibrate a permeability-enhancement parameter (e.g. our κ) to compensate for this difference, but this requires a rigorous approach that we leave for future work.

Secondly, our focus here has been on the mechanics, but the lithosphere is a region of steep thermal gradient where magma in dykes may be far from thermal equilibrium with its surroundings. Freezing may play a role in dyke propagation, but probably more important is the role that magmatic transport of sensible and latent heat plays in modifying the temperature field and hence the balance of rheological mechanisms (Bialas *et al.* 2010). Moreover, freezing (and melting) fractionates the chemistry of silicate solids and liquids, which in turn affects density, viscosity and thermodynamic phase stability; it shapes the observable geology. Our current formulation neglects thermal energy conservation and petrological thermodynamics, which is of course an area for future work. But a deeper issue is that as for the mechanisms of pressure dissipation, thermal transport through dykes occurs at scales that are not resolved by our continuum model. It remains unclear whether or how this limitation can be circumvented.

Dimensionality is another obvious limitation of the current model. The vertical plane, parallel to extension, that we use here provides a good approximation if features extend a great distance in the out-of-plane direction. But many vertical dykes associated with rifting are observed to propagate laterally, along the strike of the rift, rather than upward (Ryan 1994; Townsend *et al.* 2017). We anticipate that valuable inferences can be obtained from 2-D simulations before it is necessary to incur the computational cost of moving to three spatial dimensions. There are, moreover, other ‘dimensions’ that our models do not currently explore in terms of physics or material heterogeneity. Most prominently, we have neglected the variation of shear viscosity with temperature because we have

not included a thermochemical model. Viscosity also varies with lithology and we have neglected the chemical stratification of the lithosphere that is typically considered in rift models (e.g. Naliboff *et al.* 2017). Our plastic-strain-softening model is oversimplified, neglects healing, and lacks a thermodynamic basis (e.g. Lyakhovsky *et al.* 1997; Miehe *et al.* 2010). These physics may merit inclusion in later model development and study, but not before more fundamental aims are met and model behaviour is more deeply understood.

5 CONCLUSIONS

Motivated by an interest in melt migration from the poro-viscous mantle into the elastic/brittle crust, we have developed a mathematically consistent theory for Kelvin-viscoplastic failure of a viscoelastic medium. Our aim was to build on Keller *et al.* (2013) while addressing shortcomings in that work. To this end, our theory uses a hyperbolic plastic yield function and related potential function, and follows Duret *et al.* (2019) in introducing a Kelvin viscoplastic element to the rheological formulation.

Plasticity has long been used to approximate faulting in single-phase geodynamic models of plate tectonics. Like Keller *et al.* (2013), here we sought an analogous representation of dyking in two-phase models of solid rock and liquid magma.

The capability of our theoretical framework has been demonstrated by three investigations. First, analytical and numerical solutions were obtained for the system of ODEs that express the viscoelastic–viscoplastic rheological formulation under fixed, constant strain rates. We observed that after plastic yielding, the Kelvin viscosity introduces an internal time scale over which stress asymptotes toward steady-state values. This asymptotic stress, which exceeds the initial yield stress, increases linearly with the specified Kelvin viscosity. These ODE solutions also showed that dilatancy increases the plastic-effective pressure.

Secondly, plastic-failure modes for pure shear and tension have been demonstrated in two idealized models. The observed mesh independence of strain rates under sufficiently large Kelvin viscosity supports our hypothesis on the regularity of the rheological framework. Indeed, we have elucidated the control of the Kelvin viscosity on the behaviour of the continuum representation of a dyke. Remarkably, the stress field obtained with a pure-tensile plastic failure was shown to match the prediction by linear elastic fracture mechanics for stresses around the tip of a dyke.

Thirdly, we used a geodynamically configured model of lithosphere under imposed, horizontal extension to demonstrate the formation of faults, dykes and their interaction. In an independent confirmation of the hypothesis of Buck (2004, 2006), we showed how a dyke significantly reduces the strength of the lithosphere. This result, though preliminary, helps to establish magma-assisted plate tectonics as a quantitative hypothesis for continental and oceanic rifting. Future work using the current mathematical theory will explore the predictions associated with this hypothesis.

SUPPORTING INFORMATION

Supplementary data are available at [GJI](https://doi.org/10.1017/gji.2023.153) online.

suppl.data

Please note: Oxford University Press is not responsible for the content or functionality of any supporting materials supplied by the authors. Any queries (other than missing material) should be directed to the corresponding author for the paper.

ACKNOWLEDGMENTS

This research received funding from the European Research Council under Horizon 2020 research and innovation program grant agreement 772255. DAM acknowledges support from the National Science Foundation (NSF grant no. EAR-2121666). Numerical simulations were computed on the Arcus-C cluster from the Advanced Research Computing (ARC) services at the University of Oxford. The authors thank M. Gerbault and T. Keller for helpful discussions, and two anonymous reviewers for suggestions that improved the paper.

DATA AVAILABILITY

The source code poroVEVP is available at <https://github.com/YuanLiAC/poroVEVP>. It has dependencies on FD-PDE (Pusok *et al.* 2022b) and PETSc (Balay *et al.* 2022b). Visualization and post-processing were performed using Python and Scientific Color Maps (Cramer *et al.* 2020; Cramer 2021). Full simulation data can be provided by YL on request.

REFERENCES

- Balay, S., Gropp, W.D., McInnes, L.C. & Smith, B.F., 1997. Efficient management of parallelism in object oriented numerical software libraries, in *Modern Software Tools in Scientific Computing*, pp. 163–202, Birkhäuser Press.
- Balay, S. *et al.*, 2022a. *PETSc/TAO users manual*, Tech. Rep. ANL-21/39 - Revision 3.17, Argonne National Laboratory.
- Balay, S. *et al.*, 2022b. *PETSc Web page*, <https://petsc.org/>.
- Bedford, J.D., Faulkner, D.R., Wheeler, J. & Leclère, H., 2019. High-resolution mapping of yield curve shape and evolution for high-porosity sandstone, *J. geophys. Res.*, **124**(6), 5450–5468.
- Bialas, R.W., Buck, W.R. & Qin, R., 2010. How much magma is required to rift a continent?, *Earth planet. Sci. Lett.*, **292**(1–2), 68–78.
- Bolchover, P. & Lister, J.R., 1999. The effect of solidification on fluid-driven fracture, with application to bladed dykes, *Proc. R. Soc. Lond., A*, **455**(1987), 2389–2409.
- Borst, R. & Duret, T., 2020. On viscoplastic regularisation of strain-softening rocks and soils, *Int. J. Numer. Anal. Methods Geomech.*, **44**(6), 890–903.
- Buck, W.R., 2004. Consequences of asthenospheric variability on continental rifting, in *Rheology and Deformation of the Lithosphere at Continental Margins*, Chapter 1, pp. 1–30, Columbia Univ. Press.
- Buck, W.R., 2006. The role of magma in the development of the Afro-Arabian Rift System, *Geol. Soc., Lond., Spec. Publ.*, **259**(1), 43–54.
- Carol, I., Prat, P.C. & López, C.M., 1997. Normal/shear cracking model: application to discrete crack analysis, *J. Eng. Mech.*, **123**(8), 765–773.
- Cashman, K.V., Sparks, R. S.J. & Blundy, J.D., 2017. Vertically extensive and unstable magmatic systems: a unified view of igneous processes, *Science*, **355**(6331), eaag3055, doi:10.1126/science.aag3055.
- Chiu, P.-H. & Lin, Y.-T., 2011. A conservative phase field method for solving incompressible two-phase flows, *J. Comput. Phys.*, **230**(1), 185–204.
- Cramer, F., 2021. *Scientific Colour Maps*, Zenodo.
- Cramer, F. *et al.*, 2012. A comparison of numerical surface topography calculations in geodynamic modelling: an evaluation of the ‘sticky air’ method, *Geophys. J. Int.*, **189**(1), 38–54.
- Cramer, F., Shephard, G.E. & Heron, P.J., 2020. The misuse of colour in science communication, *Nat. Commun.*, **11**(1), 5444, doi:10.1038/s41467-020-19160-7.
- Dahm, T., 2000. Numerical simulations of the propagation path and the arrest of fluid-filled fractures in the Earth, *Geophys. J. Int.*, **141**(3), 623–638.
- Detournay, E., 2016. Mechanics of hydraulic fractures, *Ann. Rev. Fluid Mech.*, **48**, 311–339.

- Duretz, T., Borst, R. & Pourhiet, L.L., 2019. Finite thickness of shear bands in frictional viscoplasticity and implications for lithosphere dynamics, *Geochem. Geophys. Geosyst.*, **20**(11), 5598–5616.
- Duretz, T., de Borst, R., Yamato, P. & Pourhiet, L.L., 2020. Toward robust and predictive geodynamic modeling: the way forward in frictional plasticity, *Geophys. Res. Lett.*, **47**(5), doi:10.1029/2019gl086027.
- Duretz, T., Borst, R. & Yamato, P., 2021. Modelling lithospheric deformation using a compressible visco-elasto-viscoplastic rheology and the effective viscosity approach, *Geochem. Geophys. Geosyst.*, **22**(8), doi:10.1029/2021gc009675.
- Edmonds, M., Cashman, K.V., Holness, M. & Jackson, M., 2019. Architecture and dynamics of magma reservoirs, *Phil. Trans. R. Soc., A*, **377**(2139), 20180298, doi:10.1098/rsta.2018.0298.
- Fromm, J.E., 1968. A method for reducing dispersion in convective difference schemes, *J. Comput. Phys.*, **3**(2), 176–189.
- Fullsack, P., 1995. An arbitrary Lagrangian-Eulerian formulation for creeping flows and its application in tectonic models, *Geophys. J. Int.*, **120**(1), 1–23.
- Gerya, T., 2019. *Introduction to Numerical Geodynamic Modelling*, Cambridge Univ. Press.
- Heeres, O.M., Suiker, A.S. & de Borst, R., 2002. A comparison between the Perzyna viscoplastic model and the consistency viscoplastic model, *Eur. J. Mech., A*, **21**(1), 1–12.
- Iordache, M.-M. & Willam, K., 1998. Localized failure analysis in elasto-plastic cosserat continua, *Comp. Methods Appl. Mech. Eng.*, **151**(3–4), 559–586.
- Katz, R.F., 2022. *The Dynamics of Partially Molten Rock*, Princeton Univ. Press.
- Katz, R.F., Knepley, M.G., Smith, B., Spiegelman, M. & Coon, E.T., 2007. Numerical simulation of geodynamic processes with the Portable Extensible Toolkit for Scientific computation, *Phys. Earth planet. Inter.*, **163**(1–4), 52–68.
- Katz, R.F., Jones, D. W.R., Rudge, J.F. & Keller, T., 2022. Physics of melt extraction from the mantle: speed and style, *Ann. Rev. Earth planet. Sci.*, **50**, 507–540.
- Kaus, B.J., 2010. Factors that control the angle of shear bands in geodynamic numerical models of brittle deformation, *Tectonophysics*, **484**(1–4), 36–47.
- Keller, T., May, D.A. & Kaus, B. J.P., 2013. Numerical modelling of magma dynamics coupled to tectonic deformation of lithosphere and crust, *Geophys. J. Int.*, **195**(3), 1406–1442.
- Kendall, J., Stuart, G., Ebinger, C., Bastow, I. & Keir, D., 2005. Magma-assisted rifting in Ethiopia, *Nature*, **433**(7022), 146–148.
- Lanzendörfer, M., 2011. Flows of incompressible fluids with pressure-dependent viscosity (and their application to modelling the flow in journal bearing), *PhD thesis*, Mathematical Institute of Charles University.
- Lister, J.R., 1994. The solidification of buoyancy-driven flow in a flexible-walled channel. Part 2. Continual release, *J. Fluid Mech.*, **272**, 45–66.
- Liu, Z. & Buck, W.R., 2018. Magmatic controls on axial relief and faulting at mid-ocean ridges, *Earth planet. Sci. Lett.*, **491**, 226–237.
- Lorefece, R., Etse, G. & Carol, I., 2008. Viscoplastic approach for rate-dependent failure analysis of concrete joints and interfaces, *Int. J. Solids Struct.*, **45**(9), 2686–2705.
- Lyakhovsky, V., Ben-Zion, Y. & Agnon, A., 1997. Distributed damage, faulting, and friction, *J. geophys. Res.*, **102**(B12), 27 635–27 649.
- Magee, C. et al., 2018. Magma plumbing systems: a geophysical perspective, *J. Petrol.*, **59**(6), 1217–1251.
- McKenzie, D., 1984. The generation and compaction of partially molten rock, *J. Petrol.*, **25**(3), 713–765.
- Mei, S., Bai, W., Hiraga, T. & Kohlstedt, D., 2002. Influence of melt on the creep behavior of olivine–basalt aggregates under hydrous conditions, *Earth planet. Sci. Lett.*, **201**(3–4), 491–507.
- Miehe, C., Welschinger, F. & Hofacker, M., 2010. Thermodynamically consistent phase-field models of fracture: variational principles and multi-field FE implementations, *Int. J. Numer. Methods Eng.*, **83**(10), 1273–1311.
- Mirjalili, S. & Mani, A., 2020. Consistent, energy-conserving momentum transport for simulations of two-phase flows using the phase field equations, *J. Comput. Phys.*, **426**, doi:10.1016/j.jcp.2020.109918.
- Mirjalili, S., Ivey, C.B. & Mani, A., 2019. Comparison between the diffuse interface and volume of fluid methods for simulating two-phase flows, *Int. J. Multiphase Flow*, **116**, 221–238.
- Mirjalili, S., Ivey, C.B. & Mani, A., 2020. A conservative diffuse interface method for two-phase flows with provable boundedness properties, *J. Comput. Phys.*, **401**, 109006, doi:10.1016/j.jcp.2019.109006.
- Moresi, L. & Solomatov, V., 1998. Mantle convection with a brittle lithosphere: thoughts on the global tectonic styles of the Earth and Venus, *Geophys. J. Int.*, **133**(3), 669–682.
- Muller, J.R., Ito, G. & Martel, S.J., 2001. Effects of volcano loading on dike propagation in an elastic half-space, *J. geophys. Res.*, **106**(B6), 11101–11113.
- Murrell, S. A.F., 1964a. The theory of the propagation of elliptical Griffith cracks under various conditions of plane strain or plane stress: Part I, *Br. J. Appl. Phys.*, **15**(10), 1195–1210.
- Murrell, S. A.F., 1964b. The theory of the propagation of elliptical Griffith cracks under various conditions of plane strain or plane stress: Parts II and III, *Br. J. Appl. Phys.*, **15**(10), 1211–1223.
- Murrell, S. A.F. & Digby, P.J., 1970a. The theory of brittle fracture initiation under triaxial stress conditions—I, *Geophys. J. Int.*, **19**(4), 309–334.
- Murrell, S. A.F. & Digby, P.J., 1970b. The theory of brittle fracture initiation under triaxial stress conditions—II, *Geophys. J. Int.*, **19**(5), 499–512.
- Naliboff, J.B., Buiter, S. J.H., Péron-Pinvidic, G., Osmundsen, P.T. & Tetreault, J., 2017. Complex fault interaction controls continental rifting, *Nat. Commun.*, **8**(1), 1179, doi:10.1038/s41467-017-00904-x.
- Naliboff, J.B., Glerum, A., Brune, S., Péron-Pinvidic, G. & Wrona, T., 2020. Development of 3-D rift heterogeneity through fault network evolution, *Geophys. Res. Lett.*, **47**(13), doi:10.1029/2019GL086611.
- Perzyna, P., 1966. Fundamental problems in viscoplasticity, *Adv. Appl. Mech.*, **9**, 243–377.
- Pusok, A.E., Katz, R.F., May, D.A. & Li, Y., 2022a. Chemical heterogeneity, convection and asymmetry beneath mid-ocean ridges, *Geophys. J. Int.*, **231**(3), 2055–2078.
- Pusok, A.E., May, D.A., Li, Y. & Katz, R.F., 2022b. FD-PDE framework: v1.0.0.
- Renardy, M., 1986. Some remarks on the Navier-Stokes equations with a pressure-dependent viscosity, *Commun. Partial Different. Eq.*, **11**(7), 779–793.
- Rivalta, E., Taisne, B., Bungler, A. & Katz, R., 2015. A review of mechanical models of dike propagation: schools of thought, results and future directions, *Tectonophysics*, **638**, 1–42.
- Rozhko, A.Y., Podladchikov, Y.Y. & Renard, F., 2007. Failure patterns caused by localized rise in pore-fluid overpressure and effective strength of rocks, *Geophys. Res. Lett.*, **34**(22), doi:10.1029/2007GL031696.
- Rubin, A.M., 1998. Dike ascent in partially molten rock, *J. geophys. Res.*, **103**(B9), 20 901–20 919.
- Rubin, A.M. & Pollard, D.D., 1988. Dike-induced faulting in rift zones of Iceland and Afar, *Geology*, **16**(5), 413–417.
- Rudge, J.F., 2021. A micropolar continuum model of diffusion creep, *Philos. Mag.*, **101**(17), 1913–1941.
- Ryan, M.P., 1994. Neutral-buoyancy controlled magma transport and storage in mid-ocean ridge magma reservoirs and their sheeted-dike complex: a summary of basic relationships, *Int. Geophys.*, **57**, 97–138.
- Sanan, P., May, D.A., Mills, R.T., et al., 2022. DMStag: staggered, structured grids for PETSc, *J. Open Source Softw.*, **7**(79), 4531.
- Simo, J.C., Kennedy, J.G. & Govindjee, S., 1988. Non-smooth multisurface plasticity and viscoplasticity. Loading/unloading conditions and numerical algorithms, *Int. J. Numer. Methods Eng.*, **26**(10), 2161–2185.
- Spiegelman, M., May, D.A. & Wilson, C.R., 2016. On the solvability of incompressible Stokes with viscoplastic rheologies in geodynamics, *Geochem. Geophys. Geosyst.*, **17**(6), 2213–2238.
- Stathas, A. & Stefanou, I., 2022. The role of viscous regularization in dynamical problems, strain localization and mesh dependency, *Comput. Methods Appl. Mech. Eng.*, **388**, 114185, doi:10.1016/j.cma.2021.114185.

- Sun, Y. & Beckermann, C., 2007. Sharp interface tracking using the phase-field equation, *J. Comput. Phys.*, **220**(2), 626–653.
- Tackley, P.J., 2000. Self-consistent generation of tectonic plates in time-dependent, three-dimensional mantle convection simulations, *Geochem. Geophys. Geosyst.*, **1**(8), doi:10.1029/2000GC00036.
- Townsend, M.R., Pollard, D.D. & Smith, R.P., 2017. Mechanical models for dikes: a third school of thought, *Tectonophysics*, **703**, 98–118.

- Wang, W.M., Sluys, L.J. & de Borst, R., 1997. Viscoplasticity for instabilities due to strain softening and strain-rate softening, *Int. J. Numer. Methods Eng.*, **40**(20), 3839–3864.
- Wright, T.J. *et al.*, 2012. Geophysical constraints on the dynamics of spreading centres from rifting episodes on land, *Nat. Geosci.*, **5**(4), 242–250.
- Yarushina, V.M., Podladchikov, Y.Y. & Wang, L.H., 2020. Model for (de)compaction and porosity waves in porous rocks under shear stresses, *J. geophys. Res.*, **125**(8), doi:10.1029/2020jb019683.

APPENDIX A: NON-PHYSICAL STRESS WITHIN A LINEAR PLASTICITY THEORY

In the following, we illustrate how non-physical, negative deviatoric stresses may arise if the plasticity model is linear in τ_{II} . We then show how the hyperbolic plasticity model introduced can resolve this issue.

For simplicity, we neglect elasticity by assuming an infinitely large shear and bulk elastic modulus, such that a poro-viscous–viscoplastic rheological model applies. Substituting the rheological models given by eqs (5) and (8) into eqs (3) and (4) and rearranging yields

$$\left[\frac{(1-\phi)}{2\eta_\phi} + \frac{\dot{\lambda}}{2\tau_{II}} \frac{\partial Q}{\partial \tau_{II}} \right] \tau = \dot{\epsilon}, \quad \frac{(1-\phi)\Delta P}{\zeta_\phi} + \dot{\lambda} \frac{\partial Q}{\partial P_{\text{eff}}} = -C. \quad (\text{A1})$$

Taking the second invariant of both sides of the first equation in (A1), the two equations may then be written in terms of a viscous prediction and a (visco)plastic correction as

$$\tau_{II} = \tau_{II}^{\text{pred}} - \tau_{II}^{\text{corr}}, \quad \Delta P = \Delta P^{\text{pred}} - \Delta P^{\text{corr}}, \quad (\text{A2})$$

where

$$\begin{aligned} \tau_{II}^{\text{pred}} &= \frac{2\eta_\phi}{(1-\phi)} \dot{\epsilon}_{II}, & \Delta P^{\text{pred}} &= \frac{-\zeta_\phi}{(1-\phi)} C, \\ \tau_{II}^{\text{corr}} &= \frac{\eta_\phi \dot{\lambda}}{(1-\phi)} \frac{\partial Q}{\partial \tau_{II}}, & \Delta P^{\text{corr}} &= \frac{\zeta_\phi \dot{\lambda}}{(1-\phi)} \frac{\partial Q}{\partial P_{\text{eff}}}. \end{aligned} \quad (\text{A3})$$

Eq. (A2) implies that the calculation for τ_{II} and ΔP can be considered as a two-step procedure: a prediction stage to calculate τ_{II}^{pred} and ΔP^{pred} assuming that there is no plastic failure, and a correction stage to constrain the stress to lie on the Kelvin-viscoplastic yield surface by enforcing $\mathcal{F} = 0$. According to the definition of plastic-effective pressure (eq. 7), adding the same constant, ΔP^{pred} and ΔP are shifted to the values of corresponding plastic-effective pressure $P_{\text{eff}}^{\text{pred}}$ and P_{eff} , such that $P_{\text{eff}}^{\text{pred}} - P_{\text{eff}} = \Delta P^{\text{corr}}$.

Fig. 1(b) provides a geometric interpretation of eq. (A2): that of a correction path from $(P_{\text{eff}}^{\text{pred}}, \tau_{II}^{\text{pred}})$ (empty markers) to the corresponding $(P_{\text{eff}}, \tau_{II})$ (solid markers) on the yield surface. The slope of this correction path can be written as

$$k \equiv \frac{\tau_{II}^{\text{corr}}}{\Delta P^{\text{corr}}} = \frac{\eta_\phi}{\zeta_\phi} \frac{\partial Q / \partial \tau_{II}}{\partial Q / \partial P_{\text{eff}}}. \quad (\text{A4})$$

Ideally, such a path should correct any state of stresses that exceeds the plastic limit back onto the yield surface. However, using the Griffith criterion as an example, we illustrate that such a model may not result in a valid state of stresses after the correction is applied. The Griffith criterion is expressed by the following plastic yield and potential function,

$$\mathcal{F} = \tau_{II} - (P_{\text{eff}} + \sigma_t) - \eta^K \dot{\lambda}, \quad Q = \tau_{II} - c_{dl} P_{\text{eff}}, \quad (\text{A5})$$

where the dilatancy coefficient c_{dl} is a constant. If $c_{dl} = 1$, an associative plastic law applies. In the case of Griffith criterion, the slope k is constant for the entire range of parameters that is $k = -\frac{\eta_\phi}{c_{dl}\zeta_\phi}$. It is therefore immediately evident that $\tau_{II} < 0$ after correction if $P_{\text{eff}}^{\text{pred}} < -\sigma_t + \frac{\tau_{II}^{\text{pred}}}{k}$. A negative value for the second invariant of the shear stress tensor is non-physical and, as such, the corrected stress state is invalid.

This issue is resolved by using the hyperbolic plastic potential function (eq. 14). In this case, the slope of the correction path becomes

$$k = -\frac{\eta^{ve}}{\zeta^{ve} c_{dl}} \cdot \frac{\tau_{II}}{\sin \theta \sqrt{\tau_{II}^2 + (C \cos \theta - \sigma_t \sin \theta)^2}}. \quad (\text{A6})$$

Following the yield surface shown in Fig. 1(b) from larger to smaller τ_{II} , the plastic correction slope increases from a negative value until, when $\tau_{II} = 0$, the correction slope also equals zero. Such a correction path will never cross the horizontal axis and thus ensures that $\tau_{II} \geq 0$. Therefore, every point of $(P_{\text{eff}}^{\text{pred}}, \tau_{II}^{\text{pred}})$ outside the yield surface will be corrected onto a valid point on the yield surface.

By using the hyperbolic form for the yield function (eq. 10) as well as the plastic potential, we ensure that an associative plastic flow is recovered when the dilatancy coefficient $c_{dl} = 1$ in eq. (14). Furthermore, using a function for the yield surface that is smooth over the entire parameter space is beneficial for computational robustness, especially when Newton-type non-linear solvers are used.

APPENDIX B: PLASTIC-EFFECTIVE PRESSURE IN A SOLID-LIQUID CONTINUUM

To incorporate a plasticity model within the framework of a two-phase continuum model, we introduced the plastic-effective pressure. In the following we elaborate and physically justify its definition.

Table A1. Coefficients and definitions used for the two-phase implementation within the FD-PDE framework. The symbols F_g , R , M_ϕ are provided in eq. (E4).

Coefficient	Definition
A	η_{eff}
B	$-\phi F_g \hat{e}_z + \frac{\partial p^{\text{top}}}{\partial x} \hat{e}_x - \nabla \cdot \left[\frac{\eta_{\text{eff}}(1-\phi)}{G_\phi \Delta t} \mathbf{t}^o \right] + \nabla \left[\frac{\zeta_{\text{eff}}(1-\phi)}{Z_\phi \Delta t} \Delta P^o \right]$
C_m, C_p	0
D_1	$\zeta_{\text{eff}} - \frac{2}{3} \eta_{\text{eff}}$
D_2	$-R^2 M_\phi$
D_3	$F_g \hat{e}_z - \frac{\partial p^{\text{top}}}{\partial x} \hat{e}_x$
A_p, B_p	1

In a two-phase model, as Keller *et al.* (2013) argued, the definition of P_{eff} should help to address two different physical scenarios, specifically whether there is (or is not) sufficient melt to balance the solid pressure. In Keller *et al.* (2013), P_{eff} switches between these two scenarios according to an arbitrarily chosen porosity threshold. When ϕ is sufficiently large, Terzaghi's principle applies so that $P_{\text{eff}} = \Delta P$, otherwise $P_{\text{eff}} = \Delta P + P^l$, where P^l is the liquid pressure. Although such an approach is practical, the definition of P_{eff} can be elaborated in a manner that is more physically justifiable.

The key point of our argument is to appreciate the discrepancy of the fundamental assumption between the theories for plastic failure and for the two-phase continuum. In the two-phase flow theory (McKenzie 1984), each phase is assumed to be continuous on a scale of representative volume elements (RVEs). Variations below that scale are neglected. However, plasticity theories are developed on a scale smaller than that of an RVE; they are concerned with stresses acting on an existing micro-crack within the solid phase, as explained in the context of the Griffith criterion in Murrell (1964a, b). Such micro-cracks are not necessarily associated with the liquid phase, hence they do not have a direct representation in the current theory of the two-phase continuum. Therefore, careful consideration is required to combine the two theories, which intrinsically refer to physics at different length scales.

In plasticity theory, P_{eff} is the compressive stress on a micro-crack that can be one of the two types: one associated with the interconnected liquid network within the porous medium, another that is not. For the first type, Murrell & Digby (1970b) describes that the pressure of the liquid inside the microcrack exerts a tensile stress which facilitates crack opening. Thus Terzaghi's principle applies when representing this stress in the two-phase context. In this case, P_{eff} is also associated with the decompaction of the solid phase. For the second type of microcracks, P_{eff} is simply the pressure of the solid phase.

In order to use a consistent definition of P_{eff} without knowledge of the distribution of microcracks, the following two assumptions are adopted. First, the plastic-effective pressure in one RVE is an averaged value taking into account of all microcracks in the RVE, independent of whether they are microcracks of the first (fluid-filled) or second (solid-only) kind. Secondly, the ratio of microcracks of the second kind with respect to the total number of microcracks within an RVE decreases with porosity. With these two assumptions, the plastic-effective pressure takes the form of eq. (7), which involves a porosity-dependent coefficient $\alpha_p(\phi) \in [0, 1]$. When $\alpha_p = 1$, only fluid-filled microcracks are present, whereas when $\alpha_p < 1$, micro-cracks of both kinds are present.

APPENDIX C: ODE ANALYSIS FOR STRESS EVOLUTION

Here we present the analysis for the system of ODEs (eqs 18 and 19) which describe the time evolution of stresses on a material point in a poro-VEVP flow subject to an imposed strain rate.

If the rheological model contains elasticity, the stresses approach their asymptotic values after a relaxation of elastic stresses. For a viscoelastic flow, these asymptotic values are the pure viscous stresses subject to the given strain rates. For a poro-VEVP flow, the asymptotic values should satisfy eqs (18) and (19) at their steady state, that is

$$\frac{\tau_m}{\eta_\phi} + \frac{2\dot{\lambda}}{(1-\phi)} \frac{\partial Q}{\partial \tau_{II}} \bigg|_{\tau_{II}=\tau_m, \Delta P=\Delta P_m} = \frac{2\dot{\epsilon}_{II}}{(1-\phi)}, \quad (\text{C1})$$

$$\frac{\Delta P_m}{\zeta_\phi} + \frac{\dot{\lambda}}{(1-\phi)} \frac{\partial Q}{\partial P_{\text{eff}}} \bigg|_{\tau_{II}=\tau_m, \Delta P=\Delta P_m} = \frac{-C}{(1-\phi)}, \quad (\text{C2})$$

where τ_m and ΔP_m are the asymptotic shear and compaction stresses.

For a pure-shear flow, substituting the potential function eq. (14) into eq. (C1) and then eliminating $\dot{\lambda}$ by combining with the yield function in eq. (9), leads to an implicit algebraic equation for τ_m given by

$$\left[\frac{(1-\phi)}{\eta_\phi} + \frac{2}{\eta^K} \right] \tau_m - \frac{2\tau_m(C \cos \theta + P^l \sin \theta)}{\eta^K \sqrt{\tau_m^2 + (C \cos \theta - \sigma_t \sin \theta)}} = 2\dot{\epsilon}_{II}. \quad (\text{C3})$$

Eq. (C3) can be solved numerically by using the Newton's method.

Similarly, for a pure-compaction flow, an algebraic equation in terms of ΔP_m is obtained. An analytical solution exist given by

$$\Delta P_m = - \left(C + \frac{\sigma_t \sin^2 \theta}{\eta^K} \right) \left[\frac{(1-\phi)}{\zeta_\phi} + \frac{\sin^2 \theta}{\eta^K} \right]^{-1}. \quad (\text{C4})$$

In the following, we examine the temporal evolution of stress due to elasticity. Note that the stress evolution shown in this appendix concerns only the stress state after yielding.

C1 Pure-shear flow with linear yield surface

Eq. (18) is solved numerically for a pure-shear flow with the hyperbolic plasticity model. It is possible to obtain an analytical solution in the Drucker–Prager limit of the hyperbolic function at large effective pressure.

The asymptotic yield and potential functions are,

$$\mathcal{F} = \tau_{II} - (C \cos \theta + P_{\text{eff}} \sin \theta) - \eta^K \dot{\lambda}, \quad Q = \tau_{II}, \quad (\text{C5})$$

where assuming no dilatancy and zero compaction stress, then $P_{\text{eff}} = P^I$. The analytic solution is then

$$\tau_{II} = 2\eta^* \left(\dot{\epsilon}_{II} + \frac{Y}{\eta^K} \right) + \left[Y - 2\eta^* \left(\dot{\epsilon}_{II} + \frac{Y}{\eta^K} \right) \right] \exp \left[\frac{-G_\phi(t - t_b)}{\eta^*(1 - \phi)} \right], \quad \text{for } t \geq t_b \quad (\text{C6})$$

where t_b is the time of yielding and

$$\eta^* = \left[\frac{(1 - \phi)}{\eta} + \frac{2}{\eta^K} \right]^{-1}, \quad Y = C \cos \theta + P^I \sin \theta. \quad (\text{C7})$$

Accordingly, the long-term stress and the effective Maxwell timescales are

$$\tau_m = 2\eta^* \left(\dot{\epsilon}_{II} + \frac{2Y}{\eta^K} \right), \quad \tilde{t}_{\text{Mw}} = \frac{\eta^*(1 - \phi)}{G_\phi}. \quad (\text{C8})$$

It should be re-emphasized that the analytic solution in eq. (C6) is only valid when the effective pressure is sufficiently large, as it was derived using the (linear) asymptotic behaviour of the hyperbolic function.

C2 Pure-compaction flow with hyperbolic yield surface

When a pure-compaction flow is imposed, an analytic solution of eq. (19) exists when the hyperbolic plasticity model is used. The analytic solution is given by

$$\Delta P = -\zeta^* \left(C + \frac{\sigma_t \sin^2 \theta}{\eta^K} \right) + \left[\zeta^* \left(C + \frac{\sigma_t \sin^2 \theta}{\eta^K} \right) - \sigma_t \right] \exp \left[\frac{-Z_\phi(t - t_b^C)}{\zeta^*(1 - \phi)} \right], \quad \text{for } t \geq t_b^C, \quad (\text{C9})$$

where t_b^C is the time of yielding and

$$\zeta^* = \left(\frac{1 - \phi}{\zeta_\phi} + \frac{\sin^2 \theta}{\eta^K} \right)^{-1}. \quad (\text{C10})$$

Here we take the full dilatancy, that is $c_{dl} = 1$ and $P_{\text{eff}} = \Delta P$. Eq. (C9) has the same long-term stress as that given by eq. (C4). Furthermore, the effective Maxwell timescale after yielding is given by

$$\tilde{t}_{\text{Mw}}^C = (1 - \phi)\zeta^* / Z_\phi. \quad (\text{C11})$$

APPENDIX D: SEMI-DISCRETE FORMULATION

In order to implement the rheological models into the conservation of mass and momentum equations, it is convenient to introduce the effective shear and volumetric viscosity, η_{eff} and ζ_{eff} , so that the constitutive laws between the stresses and strain rates can be formulated. This is readily achieved by writing the elastic components of eq. (6) in a semi-discrete form, where by the time-derivatives of the stress are approximated using a one-step backward finite difference formulation, for example similar to Keller *et al.* (2013).

Generally, the full Jaumann objective derivative should be taken into account for the time derivatives of stresses which represent the advection and rotation. But similar to Duretz *et al.* (2021), we take a simpler approach and assume that the deformation and rotations are small, thus

$$\dot{\epsilon}^e \approx \frac{(1 - \phi)(\boldsymbol{\tau} - \boldsymbol{\tau}^o)}{2G_\phi \Delta t}, \quad C^e \approx -\frac{(1 - \phi)(\Delta P - \Delta P^o)}{Z_\phi \Delta t}, \quad (\text{D1})$$

where Δt is the time step. The superscript o denotes quantities from the previous time step.

Substituting eq. (D1) into eqs (3) and (4), the following constitutive relations are obtained

$$(1 - \phi)\boldsymbol{\tau} = 2\eta_{\text{eff}} \left[\dot{\epsilon} + \frac{(1 - \phi)\boldsymbol{\tau}^o}{2G_\phi \Delta t} \right], \quad (1 - \phi)\Delta P = -\zeta_{\text{eff}} \left[C - \frac{(1 - \phi)\Delta P^o}{Z_\phi \Delta t} \right]. \quad (\text{D2})$$

We will discuss how to compute η_{eff} and ζ_{eff} as follows. For convenience, we define the following quantities:

$$\dot{\epsilon}' = \dot{\epsilon} + \frac{(1 - \phi)\boldsymbol{\tau}^o}{2G_\phi \Delta t}, \quad C' = C - \frac{(1 - \phi)\Delta P^o}{Z_\phi \Delta t}. \quad (\text{D3})$$

Substituting the semi-discrete rheological models in eq. (D2) into eqs (3)–(4) and rearranging we obtain,

$$(1 - \phi)\tau_{II} = 2\eta^{ve} \left(\dot{\epsilon}'_{II} - \frac{\dot{\lambda}}{2} \frac{\partial Q}{\partial \tau_{II}} \right), \quad (1 - \phi)\Delta P = -\zeta^{ve} \left(C' + \dot{\lambda} \frac{\partial Q}{\partial P_{\text{eff}}} \right), \quad (\text{D4})$$

where

$$\eta^{ve} = \left(\frac{1}{\eta_\phi} + \frac{1}{G_\phi \Delta t} \right)^{-1}, \quad \zeta^{ve} = \left(\frac{1}{\zeta_\phi} + \frac{1}{Z_\phi \Delta t} \right)^{-1}, \quad \dot{\epsilon}'_{II} = [\dot{\epsilon}']_{II}. \quad (D5)$$

Therefore, the effective shear viscosity (η_{eff}) and effective volumetric viscosity (ζ_{eff}) are given by

$$(\eta_{\text{eff}}, \zeta_{\text{eff}}) := \begin{cases} (\eta^{ve}, \zeta^{ve}) & \text{if } F < 0, \\ \left(\frac{(1-\phi)\tau_{II}}{2\dot{\epsilon}'_{II}}, -\frac{(1-\phi)\Delta P}{C'} \right) & \text{if } F \geq 0. \end{cases} \quad (D6)$$

When the stresses are below the rate-independent yield surface $F < 0$ then $\dot{\lambda} = 0$ and we have poro-viscoelastic flow. When the stresses exceed the rate-independent yield stress, the state of stress is constrained to move back towards and remain on the rate-dependent yield surface such that $\mathcal{F} = 0$. The state of stresses on the yield surface and $\dot{\lambda}$ are solved for by combining eqs (D4) with the potential function in eq. (14), along with the yield function eqs (10) and the constraint that $\mathcal{F} = 0$. The approach to solving this system is explained in Sections D1 and D2.

D1 Solving for the stress on the yield surface

At the onset of plastic yielding, combining eqs (D4) and (14) and equating eq. (10) to zero results in a system of algebraic equations for $(\dot{\lambda}, \Delta P, \tau_{II})$ given by,

$$\tau_{II} = \tau_{II}^{\text{pred}} - \frac{\eta^{ve} \dot{\lambda} \tau_{II}}{(1-\phi)\sqrt{\tau_{II}^2 + A_1^2}}, \quad (D7)$$

$$\Delta P = \Delta P^{\text{pred}} + \frac{c_{dl} \zeta^{ve} \dot{\lambda} \sin \theta}{(1-\phi)}, \quad (D8)$$

$$\sqrt{\tau_{II}^2 + A_1^2} - (A_2 + \Delta P \sin \theta) - \eta^K \dot{\lambda} = 0, \quad (D9)$$

where

$$\tau_{II}^{\text{pred}} = 2\eta^{ve} \dot{\epsilon}'_{II}, \quad \Delta P^{\text{pred}} = -\zeta^{ve} C', \quad A_1 = C \cos \theta - \sigma_t \sin \theta, \quad A_2 = C \cos \theta + (1 - \alpha_p) P^l \sin \theta. \quad (D10)$$

Eqs (D7) and (D8) can be rewritten in the form $\dot{\lambda} = \dot{\lambda}(\tau_{II})$ and $\Delta P = \Delta P(\tau_{II})$, respectively. Substituting these expressions into eq. (D9) leads to an equation only in terms of τ_{II} which has to be solved numerically. We use Newton's method to solve the local (point-wise) non-linear problem. Its initial guess is formulated from an analytical solution of (D9) in terms of τ_{II} by making the approximation,

$$\sqrt{\tau_{II}^2 + A_1^2} \sim \tau_{II} + A_1. \quad (D11)$$

D2 Numerical procedure for global and local convergence

The stress must satisfy both the conservation of mass and momentum (global equations) in addition to the constraints imposed by the plasticity model (local equations). The global convergence is achieved by using a standard Newton type method to solve eqs (24) and (25), while the local solve is nested within each global iteration to update the effective viscosities, η_{eff} and ζ_{eff} , on each grid point for the global solver following the rules in eq. (D6).

The local solver takes the following procedure on each grid point. Given τ^o , ΔP^o , v^s , P^l ,

- (i) Compute η^{ve} and ζ^{ve} that assumes a poro-viscoelastic rheological model.
- (ii) Compute ΔP^{pred} , τ_{II}^{pred} that the strain rates are computed from v^s obtained in the previous step.
- (iii) Compute $F(\tau_{II}^{\text{pred}}, \Delta P^{\text{pred}})$.

(a) If $F < 0$, set $\eta_{\text{eff}} = \eta^{ve}$ and $\zeta_{\text{eff}} = \zeta^{ve}$.

(b) If $F \geq 0$, solve eqs (D7)–(D9) for τ_{II} , ΔP , $\dot{\lambda}$, then obtain η_{eff} , ζ_{eff} using the rule in eq. (D6) for the nonlinear case.

APPENDIX E: NON-DIMENSIONALIZATION

In this section, we introduce the non-dimensionalization used to scale the governing equations prior to discretization and numerical solution. Simulation results are then re-dimensionalized before they are plotted in this paper.

Denoting the characteristic length and velocity scale as L and U and choosing a reference viscosity as η_{ref} , then the characteristic stress is $\eta_{\text{ref}} U/L$. Using these three characteristic scales, we define the following scaling relationships: $v^s = U v'$, $\mathbf{x} = L \mathbf{x}'$, $t = (L/U) t'$, $\nabla = (1/L) \nabla'$, $(\eta_{\text{eff}}, \zeta_{\text{eff}}) = \eta_{\text{ref}} (\eta'_{\text{eff}}, \zeta'_{\text{eff}})$, $(P^l, \Delta P^o, p^{\text{top}}, \tau^o) = (\eta_{\text{ref}} U/L)(p', \Delta P'^o, p'^{\text{top}}, \tau'^o)$ and $(G_\phi, Z_\phi) = (\eta_{\text{ref}} U/L)(G'_\phi, Z'_\phi)$ in which the primed variables denote non-dimensional quantities. Using these expression the non-dimensionalized semi-discrete equations can be written as

$$\begin{aligned} & -\nabla' p' + \nabla' \cdot \left[\eta'_{\text{eff}} (\nabla' v' + \nabla' v'^T) \right] + \nabla' \cdot \left[\left(\zeta'_{\text{eff}} - \frac{2}{3} \eta'_{\text{eff}} \right) \nabla' \cdot v' \right] \\ & + \phi F_s \hat{e}_z - \frac{\partial p'^{\text{top}}}{\partial x'} \hat{e}_x + \nabla' \cdot \left[\frac{\eta'_{\text{eff}} (1-\phi)}{G'_\phi \Delta t'} \tau'^o \right] - \nabla' \cdot \left[\frac{\zeta'_{\text{eff}} (1-\phi)}{Z'_\phi \Delta t'} \Delta P'^o \right] = \mathbf{0}, \end{aligned} \quad (E1)$$

$$\nabla' \cdot \mathbf{v}' - \nabla' \cdot R^2 M_\phi \left(\nabla' p' - F_g \hat{\mathbf{e}}_z + \frac{\partial p'^{\text{top}}}{\partial x'} \hat{\mathbf{e}}_x \right) = 0, \quad (\text{E2})$$

$$\frac{\partial(1-\phi)}{\partial t'} + \nabla' \cdot (1-\phi) \mathbf{v}' = 0, \quad (\text{E3})$$

where $\hat{\mathbf{e}}_z$ and $\hat{\mathbf{e}}_x$ denote the unit vector in the vertical and the horizontal direction, respectively. The other non-dimensional parameters introduced are

$$F_g = \frac{\Delta \rho g L^2}{\eta_{\text{ref}} U}, \quad M_\phi = \frac{\phi^3}{(1-\phi)^2}, \quad R = \frac{\delta}{L}, \quad \delta = \sqrt{\eta_{\text{ref}} M_0}. \quad (\text{E4})$$

APPENDIX F: PHASE-FIELD METHOD FOR FREE SURFACE

We model the free surface of the rock as an interface with a layer of ‘sticky air’ (Cramer *et al.* 2012). We use the phase-field method (Mirjalili *et al.* 2019, 2020; Mirjalili & Mani 2020) to describe the interface between sticky air and material associated with the poro-VEVP domain. The benefit of the phase-field method is that the interface can be represented as a contour of a continuum field. A discussion of theory of the phase-field method, its implementation for generic interface tracking, and benchmarks can be found in Mirjalili & Mani (2020) and references therein. Helpfully, Mirjalili & Mani (2020) investigate the boundedness and stability criterion of this approach. We recapitulate the key elements of the method below, and then explain our approach to capture the subgrid displacement of the free surface.

The phase-field method uses a field $f(\mathbf{x}) \in (0, 1)$ to describe the coexistence of more than one material region (i.e. ‘phase’) in terms of a continuous variable in a domain.¹ More specially, for a domain containing two regions separated by an interface, the field value represents a continuous variation from one region $f \approx 0$ to another region $f \approx 1$. The interface is defined by the contour $f = 0.5$. The field, $f(\mathbf{x})$ is defined following a kernel function

$$f(x_n) = \frac{1}{2} \left[1 + \tanh \left(\frac{x_n}{2\epsilon} \right) \right], \quad (\text{F1})$$

where ϵ controls the width of the transition between regions and x_n is a signed distance from the interface. With the prescription of an initial interface, the field f is initialized accordingly using eq. (F1). At subsequent times f evolves according to a non-linear advection–diffusion equation,

$$\frac{\partial f}{\partial t} + \nabla \cdot (f \mathbf{v}) = \nabla \cdot \left[\gamma \left(\epsilon \nabla f - f(1-f) \frac{\nabla f}{|\nabla f|} \right) \right], \quad (\text{F2})$$

where γ is a numerical constant chosen as a function of the maximum magnitude of the velocity. The contour $f = 0.5$ is found for every time step to update the position of interface.

In our 2-D, staggered-grid, finite difference implementation we use a Cartesian grid consisting of $M \times N$ cells, with the size Δx , Δz in the x , z direction, respectively. We use a value of $\epsilon = 0.7 \Delta z$. If ϵ is too large, the diffusion term in eq. (F2) may alter the shape of interface. If ϵ is too small, the boundedness condition can be violated (Mirjalili & Mani 2020). Following Mirjalili & Mani (2020) we choose $\gamma = \max(|\mathbf{v}|)$ and evolve eq. (F2) using $\Delta t_{\text{pf}} < \epsilon/2\gamma$. In practice, this step-size limit is larger than the one required for the simulation of plastic failure.

It is possible to capture the subgrid scale displacement of the free surface at each time step. We achieve this by (i) approximating the location of the sharp interface to first-order accuracy of the subgrid scale using f , then (ii) use the sharp interface to compute the volume fraction of each region (sticky air material versus the poro-VEVP material) within each cell.

To compute the sharp interface we approximate the interface as a set of straight-line segments. A staggered finite difference cell defines phase-field values on faces; a linear interpolation across the neighbour cells gives the values on vertices of the cell, f_i , $i = 1, 2, 3, 4$. If a cell is associated with values f_i that span 0.5 then we assume that this cell contains a piece of interface; we approximate this piece as a straight line. For these interface-cut cells, we use the values of f at the midpoint of all four faces and then use the inverse of eq. (F1) to define a value of x_n at each midpoint. Thus the location of the line-segment in the cell can be calculated according to the location of these midpoints and the distance from them to the line. From this, the volume of the two regions within the cell that are separated by the interface can be determined. Furthermore, as x_n is a signed distance it is immediately known to which material region the subvolume is associated with.

APPENDIX G: SOLVABILITY

Here we discuss the solvability of the plasticity model presented in this paper. Our analysis focuses on the solvability under plastic failure in the incompressible limit. This limit is relevant for shear failure occurring at zero porosity in a Stokes–Darcy model, for example the pure shear failure example in Section 3.2.1 and the tectonic-scale model in Section 3.3.

Renardy (1986) first identified that the stationary (Navier–)Stokes equation may become ill-posed due to a lose of ellipticity of the governing equations if the effective viscosity depends on pressure. The condition required to maintain ellipticity is that all eigenvalues λ_k of $\partial \boldsymbol{\tau} / \partial P$ must satisfy $\lambda_k < 1$. Lanzendörfer (2011) extended the theory to allow the viscosity to depend on both the strain rate and pressure, and proved that the well-posedness condition is

$$\left\| \frac{\partial \boldsymbol{\tau}}{\partial P} \right\| \leq \Theta, \quad \Theta < 1. \quad (\text{G1})$$

¹To avoid potential confusion with the usage of the word ‘phase’ in light of the two-phase continuum formulation, we opt to use the word ‘region’.

Lanzendörfer (2011) finds that a numerical calculation may still fail even when this condition is satisfied if Θ is close to one. The author suggests the reason is that intermediate steps within each iteration may violate this condition. For example, in some numerical experiments in Lanzendörfer (2011), Θ can be as low as ~ 0.7 when the numerical convergence fails because of ill-posedness. Spiegelman *et al.* (2016) uses this condition to demonstrate that there is an inherent solvability issue in the mathematical equation for a viscoplastic flow with a Drucker–Prager yield condition.

In the following we show that an improvement on this issue can be achieved by using the VEP rheological model. First, we rewrite eq. (G1) in terms of the stress invariant, that is

$$\frac{\partial \tau_{II}}{\partial P} \leq \frac{\sqrt{2}}{2} \Theta, \quad \Theta < 1. \quad (\text{G2})$$

At zero porosity, we have that $P_{\text{eff}} = P$ and there is no dilatancy, hence the system (D7)–(D9) simplifies to

$$\tau_{II} = \tau_{II}^{\text{pred}} - \eta^{ve} \dot{\lambda} \frac{\partial Q}{\partial \tau_{II}}, \quad (\text{G3})$$

$$\sqrt{\tau_{II}^2 + (C \cos \theta - \sigma_t \sin \theta)^2} - \left[C \cos \theta + \left(P + \frac{\eta^K \dot{\lambda}}{\sin \theta} \right) \sin \theta \right] = 0, \quad (\text{G4})$$

where we recall the plastic potential function is given by $Q = \sqrt{\tau_{II}^2 + (C \cos \theta - \sigma_t \sin \theta)^2}$.

Eq. (G4) can be rewritten in the form $\tau_{II} = \tau_{II}(P)$. Differentiating this expression with respect to P , we obtain

$$\frac{\partial \tau_{II}}{\partial P} = \left(1 + \frac{\eta^K}{\sin \theta} \frac{\partial \dot{\lambda}}{\partial P} \right) \mathcal{G} \left(P + \eta^K \dot{\lambda} / \sin \theta \right), \quad (\text{G5})$$

where $\mathcal{G} \left(P + \eta^K \dot{\lambda} / \sin \theta \right)$ is a known but somewhat messy function. Differentiating eq. (G3) with respect to P ,

$$\frac{\partial \tau_{II}}{\partial P} = -\eta^{ve} \left(\frac{\partial Q}{\partial \tau_{II}} \frac{\partial \dot{\lambda}}{\partial P} + \dot{\lambda} \frac{\partial^2 Q}{\partial \tau_{II}^2} \frac{\partial \tau_{II}}{\partial P} \right), \quad (\text{G6})$$

and rearranging this gives

$$\frac{\partial \dot{\lambda}}{\partial P} = -\frac{1}{\partial Q / \partial \tau_{II}} \left(\frac{1}{\eta^{ve}} + \dot{\lambda} \frac{\partial^2 Q}{\partial \tau_{II}^2} \right) \frac{\partial \tau_{II}}{\partial P}. \quad (\text{G7})$$

Substituting eq. (G7) into (G5) gives

$$\frac{\partial \tau_{II}}{\partial P} = \left[\frac{1}{\mathcal{G}} + \frac{\eta^K}{\sin \theta} \left(\frac{1}{\eta^{ve} \partial Q / \partial \tau_{II}} + \dot{\lambda} \frac{\partial^2 Q}{\partial \tau_{II}^2} \right) \right]^{-1}. \quad (\text{G8})$$

Whilst it is not straightforward to argue that eq. (G8) will satisfy the well-posedness condition (G2) in general, there are two observations that provide a guide for parameter selection to enhance solvability and hence robustness of simulations.

First, increasing η^K / η^{ve} will reduce the value of $\partial \tau_{II} / \partial P$. However, increasing η^K affects the dynamics predicted by model solutions. In contrast, η^{ve} can be decreased by reducing the time step size Δt , as evident from the definition of η^{ve} in eq. (D5). The fact that decreasing Δt can be used to control the magnitude of $\partial \tau_{II} / \partial P$ and hence promote solvability implies that elasticity is important in maintaining the well-posedness of the problem (Keller *et al.* 2013).

Secondly, for a hyperbolic yield surface, $\partial \tau_{II} / \partial P$ has an asymptotic minimum when $\tau_{II} \gg C \cos \theta - \sigma_t \sin \theta$. At this minimum value, we have

$$\sqrt{\tau_{II}^2 + (C \cos \theta - \sigma_t \sin \theta)^2} \sim \tau_{II} + (C \cos \theta - \sigma_t \sin \theta). \quad (\text{G9})$$

Inserting eq. (G9) into eq. (G4) and following the procedure as before we obtain

$$\frac{\partial \tau_{II}}{\partial P} \geq \frac{\eta^{ve}}{\eta^{ve} + \eta^K} \sin \theta. \quad (\text{G10})$$

Again eq. (G10) emphasizes that reducing the time step Δt is a valid means to maintain the well-posedness condition for the parameter range of interest.

As a comparison, Spiegelman *et al.* (2016) suggests that the well-posedness condition for a viscoplastic flow with a Drucker–Prager criteria is determined by the value of $(C \cos \theta + P \sin \theta)(2\eta \dot{\epsilon}_{II})^{-1}$ when a harmonic style of effective viscosity is applied. The larger this value is, the less likely the solvability condition is violated. However, unlike the VEP rheological model, there is no way to control the value of $\partial \tau_{II} / \partial P$ without changing the physical parameters and thus changing the dynamics of the physical problem.

It should be noted that the ellipticity condition discussed above applies strictly to incompressible materials. It is not clear whether the results of our analysis apply to the Stokes–Darcy model, since the structure of the partial differential equations differs from the incompressible case. In particular, whilst in both cases the differential operator applied to the velocity is second order, the differential operator applied to pressure is first order in the case of an incompressible material and second order in the case of the Stokes–Darcy model. Nonetheless, the lack of mesh-dependent features in Section 3.2.2 indicates the robustness of our poro-VEP formulation within a Stokes–Darcy model.

APPENDIX H: FD-PDE

The FD-PDE library (Pusok *et al.* 2022a, b), a software layer on top of PETSc (Balay *et al.* 2022b), provides a reproducible and extensible framework for solving a single-/two-phase system with complex rheological models. Its core module discretizes the partial differential equations on a 2-D, Cartesian staggered grid. In this work, the standard form used to describe the conservation of mass and momentum for the two-phase system is given as

$$-\nabla P^l + \nabla \cdot [A(\nabla \mathbf{v}^s + (\nabla \mathbf{v}^s)^T)] + \nabla (D_1 \nabla \cdot \mathbf{v}^s) - \mathbf{B} = \mathbf{0}, \quad (\text{H1})$$

$$\nabla \cdot \mathbf{v}^s + \nabla \cdot (D_2 \nabla P + \mathbf{D}_3) - C_m = 0, \quad (\text{H2})$$

$$A_p \left[\frac{\partial Q}{\partial t} + \nabla \cdot (\mathbf{v}^s Q) \right] - \nabla \cdot (B_p \nabla Q) + C_p = 0. \quad (\text{H3})$$

The unknowns are denoted as P^l , \mathbf{v}^s and Q and in our model, correspond to the liquid pressure, the solid velocity and the solid fraction $Q = 1 - \phi$. The definition of the coefficients A , \mathbf{B} , C_m , C_p , D_1 , D_2 , \mathbf{D}_3 , A_p , B_p used in our model are provided in Table A1. Note, A , \mathbf{B} and D_1 all are non-linear coefficients because of η_{eff} and ζ_{eff} .

A line-search-based Newton solver is used to solve the discretized system of non-linear equations. The Jacobian matrix required for each Newton iteration is calculated numerically via graph colouring and a finite-difference approximation involving a perturbation of the non-linear residual defined by eqs (H1)–(H3).